

1 **The Impact of Parameterized Lateral Mixing on the Antarctic Circumpolar**
2 **Current in a Coupled Climate Model**

3 Sarah Ragen*

4 *University of Washington School of Oceanography, Seattle, Washington.*

5 Marie-Aude Pradal

6 *Johns Hopkins University Department of Earth and Planetary Sciences, Baltimore, Maryland*

7 Anand Gnanadesikan

8 *Johns Hopkins University Department of Earth and Planetary Sciences, Baltimore, Maryland*

9 *Corresponding author address: School of Oceanography, University of Washington, 1492 NE

10 Boat St., Seattle, WA.

11 E-mail: sragen@uw.edu

ABSTRACT

12 This study examines the impact of changing the lateral diffusion coefficient
13 A_{Redi} on the transport of the Antarctic Circumpolar Current (ACC). The ACC
14 is difficult to accurately simulate in climate models. A_{Redi} is poorly con-
15 strained with values ranging across an order of magnitude in climate models.
16 Moreover, there is a large spread in eastward transport in the Southern Ocean
17 (SO) in climate models. This paper examines how much of that spread can
18 be attributed to different eddy parameterization coefficients. A coarse resolu-
19 tion, fully coupled model suite was run with $A_{Redi} = 400 \text{ m}^2 \text{ s}^{-1}$, $800 \text{ m}^2 \text{ s}^{-1}$,
20 $1200 \text{ m}^2 \text{ s}^{-1}$, and $2400 \text{ m}^2 \text{ s}^{-1}$. Additionally, two simulations were run with
21 two-dimensional representations of the mixing coefficient based on satellite
22 altimetry. Relative to the $400 \text{ m}^2 \text{ s}^{-1}$ case, the $2400 \text{ m}^2 \text{ s}^{-1}$ case exhibits a)
23 an 11% decrease in average wind stress from 50-65°S, b) a 24% decrease in
24 zonally averaged eastward transport in the SO, and c) a 14% weaker transport
25 through the Drake Passage. The decrease in transport is well explained by
26 changes in the thermal wind shear, largely due to increases in ocean density
27 occurring on the northern side of the ACC. In intermediate waters these in-
28 creases are associated with changes in the formation of intermediate waters in
29 the North Pacific. We hypothesise that the deep increases are associated with
30 changes in the wind stress curl allowing Antarctic Bottom Water to escape
31 and flow northwards.

32 **1. Introduction**

33 Processes in the Southern Ocean play a significant role in the global meridional overturning
34 circulation and the stratification of the global ocean (Naveira Garabato et al. 2016; Karsten and
35 Marshall 2002; Gnanadesikan and Hallberg 2000). These processes are strongly influenced by the
36 only ocean current that completely encircles the globe. The Antarctic Circumpolar Current (ACC)
37 flows around Antarctica from west to east, tracing a roughly 25,000 km path around the world
38 (Rintoul 2009). In terms of volume transport, the ACC is the largest ocean current on Earth, with
39 observational estimates at Drake Passage ranging from 134 Sv (Whitworth and Peterson 1985;
40 Cunningham et al. 2003) to 173.3 ± 10.7 Sv (Donohue et al. 2016). Moreover, as the only current
41 that circumnavigates the Earth unimpeded by land, the ACC is unique in its role as a mechanism
42 for mixing water masses that originate in different ocean basins (Worthington 1981) and is a vital
43 component of the global general ocean circulation.

44 Due to the sheer volume of water transported by the ACC and its proximity to sea ice and
45 Antarctic ice sheets, its dynamics are particularly important for climate. The ACC's large capacity
46 for heat uptake and its influence on the meridional overturning circulation make it an important
47 driver for salinity, heat and carbon redistribution in the global ocean system (Giglio and Johnson
48 2016; Frölicher et al. 2015). The observed and projected regional trends in Antarctic ice sheet
49 melting are likely due to oceanic forcing and advection of heat (Alley et al. 2015) associated
50 with changes in the circulation of the ACC. Changes in temperature and salinity of Southern
51 Ocean water masses could have large repercussions for ocean circulation, sea level rise, and global
52 climate (Alley et al. 2005; Pritchard et al. 2012). In addition to its role in the melting of sea ice and
53 ice sheets, the Southern Ocean is an important sink for anthropogenic carbon (Caldeira and Duffy
54 2000; Frölicher et al. 2015). The Southern Ocean takes up over one quarter of anthropogenic

55 carbon each year, slowing the rate of global warming. This relatively high uptake of CO₂ does
56 not correspond with higher levels of carbon storage, as the carbon taken up in the Southern Ocean
57 is exported northward isopycnally to other reservoirs (Caldeira and Duffy 2000; Ito et al. 2010;
58 Gnanadesikan et al. 2015b).

59 Multiple physical processes, both global and specific to the Southern Ocean (SO), influence the
60 transport of the ACC. The westerly winds over the SO impart momentum to the ACC, which flows
61 unimpeded by topography at shallow depths. In the zonal mean, this momentum is balanced by
62 form drag at depth (Gille 1997; Hallberg and Gnanadesikan 2001). This implies that the northward
63 Ekman flux at the surface must be balanced by a southward geostrophic flux of waters below the
64 depth of topographic features in the SO. A number of authors have used this momentum balance
65 to predict a barotropic ACC in which the transport scales as the wind stress (Munk and Palmén
66 1951; Wang 1994). However, the ACC is far from barotropic. As the Ekman flow is lighter than
67 the deep inflow, the resulting circulation is associated with a tilting of isopycnals that slope down
68 away from the continent, resulting in a thermal wind shear across the current.

69 There are several physical regimes in which the northward Ekman and southward deep flows
70 balance (Hallberg and Gnanadesikan 2001), resulting in different relationships between the ther-
71 mal wind shear in the current and the large scale overturning. The first regime involves connecting
72 the deep and shallow flows through surface buoyancy transformation. Southward flowing water
73 upwells in the Southern Ocean, is initially lightened via freshening, warms as it moves northward
74 and then is injected into the thermocline as mode and intermediate water (Gnanadesikan 1999;
75 Gnanadesikan and Hallberg 2000). The thermal wind shear is then determined both by the density
76 contrast across the current, $\Delta\rho$, (Fučkar and Vallis 2007) and by the relationship between the py-
77 cnocline and Northern Hemisphere overturning - if as in Gnanadesikan (1999) the overturning in

78 the north depends on $\Delta\rho$ and the square of the pycnocline depth D , for fixed $\Delta\rho$, $D \propto \sqrt{\tau}$ and the
79 ACC transport scales as windstress τ .

80 It is quite clear, however, that the Northern Hemisphere overturning is smaller than the Ekman
81 flux in the Southern Ocean, and that not all of the upwelling water is drawn from deeper levels.
82 There are two possible mechanisms by which this can occur. The first is the formation of station-
83 ary eddies, whereby dense water is mounded up over ridges as the ACC deflects northward over
84 topographic features (which can be seen in hydrography in many parts of the ocean). This can
85 result in a potentially significant fraction of the southward flow returning as northward flow over
86 these ridges (Hallberg and Gnanadesikan 2001).

87 A second way of limiting the amount of deep upwelling is the presence of transient eddies. In a
88 flat-bottomed channel, the overturning produced by a zonal wind stress steepens tilting isopycnals
89 and increases thermal wind shear up to the point where the flow becomes baroclinically unstable
90 (Johnson and Bryden 1989; Straub 1993). Beyond this point, eddies generate an advective over-
91 turning that acts to strongly restore the flow to a level of marginal instability, largely balancing
92 any changes in the wind-driven overturning. In such a regime, the transport is constrained below
93 some maximum value. Such eddy-saturation has been found in idealized eddy-permitting models
94 with topography that do not include buoyancy forcing (Tansley and Marshall 2001; Munday et al.
95 2013) and is approximately found in realistic eddy-permitting models of the Circumpolar Current
96 which are run out for relatively short periods of time (Hallberg and Gnanadesikan 2006).

97 However, as noted by Jones et al. (2011), the timescale for the low-latitude pycnocline to adjust
98 to any imbalance between the Ekman-driven overturning and the eddy flux that compensates it (i.e.
99 to changes in the so-called residual flow) can be many hundreds of years. Thus, the degree to which
100 the actual ACC is in a saturation regime may be overestimated. Hallberg and Gnanadesikan (2001)
101 presented an idealized model that included each of the aforementioned three methods of closing

102 the Southern Ocean Ekman flux and found three stable regimes: a buoyancy forcing dominated
103 regime, an eddy-compensation regime in which eddies compensate a relatively constant fraction
104 of the overturning, and an eddy-saturation regime in which increases in Ekman flux are balanced
105 by increases in the eddy overturning. In the first regime, fractional changes in the wind stress
106 match fractional changes in the ACC transport. In the second regime, fractional changes in the
107 wind stresses are associated with smaller fractional changes in the transport. In third regime, the
108 transport is insensitive to wind stress but the eddy energy increases with wind stress (Meredith
109 and Hogg 2006). Hallberg and Gnanadesikan (2001) argued that the real world falls in the second
110 regime and a number of model studies since then have been consistent with this prediction (Dufour
111 et al. 2012; Morrison and McC. Hogg 2013; Langlais et al. 2015; Doddridge et al. 2019).

112 In most coupled climate models, mesoscale eddies cannot be directly simulated as they occur
113 at spatial scales smaller than the model grids. To account for the impact of these eddies, climate
114 models employ two eddy parameterization schemes, referred to as the Redi scheme and the Gent-
115 McWilliams scheme. Both are schematically illustrated in Fig. 1. The Gent-McWilliams scheme
116 (Fig. 1, left-hand side) represents the eddy compensation using a diffusion coefficient A_{GM} (Gent
117 and McWilliams 1990). Horizontal fluxes then take the form $F_C = -A_{GM} \frac{\partial S}{\partial z} C$ where S is the slope
118 of the isopycnal and C is the concentration of the tracer being transported.

119 The Redi parameterization (Fig. 1, right-hand side) refers to mixing along neutral surfaces with
120 diffusion coefficient A_{Redi} (Redi 1982) and fluxes given by $F_C = -A_{Redi} \nabla_h C$, where $\nabla_h C$ repre-
121 sents the lateral tracer gradient. The actual value of A_{Redi} in the Southern Ocean is uncertain.
122 Many studies and papers prescribe identical values for A_{Redi} and A_{GM} (Griffies 1998; Gnanade-
123 sikan et al. 2006). However, this strategy necessitates using relatively small mixing coefficients
124 since GM coefficients greater than $1000 \text{ m}^2 \text{ s}^{-1}$ damp the overturning circulation (Gnanadesikan
125 1999). Spatiotemporally constant values of A_{Redi} used in CMIP5 models range from $500 \text{ m}^2 \text{ s}^{-1}$

126 (Johns et al. 2006) to $2000 \text{ m}^2 \text{ s}^{-1}$ (Fogli et al. 2009). Other models use spatially varying A_{Redi}
127 ranging from values of around $200 \text{ m}^2 \text{ s}^{-1}$ in gyres and 650 to $1500 \text{ m}^2 \text{ s}^{-1}$ in boundary currents
128 (Gnanadesikan et al. 2006; Dunne et al. 2012; Bentsen et al. 2013). However, observational esti-
129 mates of A_{Redi} ranging from 1000 to more than $10,000 \text{ m}^2 \text{ s}^{-1}$ have been obtained using floats and
130 tracers (Ledwell et al. 1998; Gnanadesikan et al. 2013; Lumpkin and Flament 2001) whereas esti-
131 mates from satellite altimetry range from less than 200 to more than $10,000 \text{ m}^2 \text{ s}^{-1}$ (Abernathey
132 and Marshall 2013).

133 The transport of the ACC is often poorly simulated in climate models (Russell et al. 2006;
134 Beadling et al. 2019). Values in the CMIP3 archive for the transport at Drake Passage range from
135 50 - 300 Sv with a mean transport of $144.6 \pm 74.1 \text{ Sv}$. CMIP5 gives a slightly better range, putting
136 transport at Drake Passage in a range from 88 - 246 Sv with a mean transport of $155 \pm 51 \text{ Sv}$
137 (Meijers et al. 2012; Meijers 2014; Beadling et al. 2019).

138 The reasons for these differences remain obscure. Beadling et al. (2019) shows that the maxi-
139 mum wind stress by itself explains relatively little intermodel variability, while the density gradient
140 across the ACC explains much of the variability. However, so many things change between models
141 (ocean mixing, cloud parameterizations, atmosphere gravity wave drag, atmospheric and oceanic
142 resolution, sea ice models) that it is difficult to isolate which processes have the most important
143 role. To date, only a few studies have isolated the impact of changing eddy parameterization. Gent
144 et al. (2001) presented a study in which winds and the mixing coefficients $A_{GM} = A_{Redi}$ were both
145 varied in a coupled model. They found that increasing the mixing coefficients together decreased
146 the strength of the current. This is expected as the eddy overturning associated with the GM co-
147 efficient scales as $A_{GM} \cdot S$, and thus with a larger coefficient a smaller isopycnal slope S would be
148 required for the eddy flux to balance the Ekman flux. This in turn would imply a lower thermal
149 wind shear. For a fixed A_{GM} coefficient, however, the overturning and ACC transport were found

150 to increase with the wind stress. Similarly, Farneti and Gent (2011) found that the details of the
151 GM parameterization, in particular the value at which A_{GM} is limited so as to avoid singularity in
152 mixed layers can also affect the ability of the eddy advection to realistically compensate changes
153 in the Ekman flux.

154 Insofar as A_{Redi} primarily mixes along isopycnals, warming or cooling along isopycnals should
155 be balanced by salinification or freshening. It might therefore be assumed that changing A_{Redi}
156 would not significantly alter isopycnal slopes and thus would have a relatively limited impact on
157 the ACC, so that one could attribute the sensitivity seen by Gent et al. (2001) entirely to the A_{GM}
158 coefficient. However, as we will demonstrate in this paper, when A_{Redi} is allowed to vary in-
159 dependently of A_{GM} over a range comparable to that seen within the CMIP5 ensemble within a
160 single coupled climate model it can have a significant impact on the ACC. This is both because
161 such changes in A_{Redi} produce changes in SSTs (Pradal and Gnanadesikan 2014) which in turn
162 impact the winds over the SO, as well as because they produce changes in high latitude stratifica-
163 tion and convection. In the following section of this paper, we will introduce the model used and
164 the experimental design. Section 3 presents the results of six different simulations with different
165 representations of A_{Redi} , allowing us to evaluate how much of the range seen in CMIP5 could be
166 attributed to variations in this parameterization. In the last section of the paper, we will discuss
167 what our results imply about the dynamics of the Circumpolar Current.

168 **2. Model description**

169 For this study, the physical model used is the Geophysical Fluid Dynamics Laboratory (GFDL)
170 fully coupled CM2Mc (Coupled Model 2 with Modular Ocean, coarse grid). The model includes
171 separate atmosphere, ocean, sea ice, and land components that are linked through a flux coupler.
172 The atmosphere model grid consists of 24 vertical levels, with a 3.75° longitudinal resolution

173 and a 3° latitudinal resolution. The ocean model has 28 vertical levels and a nominal $3^\circ \times 1.5^\circ$
174 resolution, with a latitudinal resolution which is finer in the equatorial waveguide and in Drake
175 Passage latitudes. The model contains up-to-date representations of many processes, including
176 atmospheric convection, oceanic vertical mixing, and eddy mixing. Climatological annual cycles
177 of ozone and twelve classes of aerosols (black carbon, sulfate, organic carbon, sea salt and eight
178 size classes of dust) are prescribed. Additionally, global mean atmospheric concentrations of three
179 greenhouse gasses (CO_2 , CH_4 and N_2O) are fixed throughout the run.

180 Four simulations were conducted with the diffusive eddy mixing coefficient A_{Redi} set to spa-
181 tiotemporally constant values of $400 \text{ m}^2 \text{ s}^{-1}$, $800 \text{ m}^2 \text{ s}^{-1}$, $1200 \text{ m}^2 \text{ s}^{-1}$, and $2400 \text{ m}^2 \text{ s}^{-1}$. These
182 runs are referred to as AREDI400, AREDI800, AREDI1200 and AREDI2400 respectively. Ad-
183 ditionally, two simulations were made in which the A_{Redi} was estimated using a field of surface
184 velocities estimated from satellite altimetry (Abernathey and Marshall 2013). The resulting field
185 of A_{Redi} is shown in Fig. 2a and shows relatively small values in the Southern Ocean but much
186 higher values in the subtropical gyres. A simulation made with this field is referred to as ABER2D.
187 To evaluate whether changes due to employing this 2D field were due to the full 2D structure of
188 the field or merely to the latitudinal variation in the field, an additional simulation was made with
189 a zonally-averaged version of Fig. 2a, shown in Fig. 2b and referred to as ABERZONAL. We
190 note that the fields are both isotropic and independent of depth, conditions that are unlikely to hold
191 in the real world. However, there is no consensus in the literature for how diffusion coefficients
192 should fall off with depth and previous work (Gnanadesikan et al. 2015a) suggests relatively high
193 coefficients in the deep Southeast Pacific. Our results should thus be taken as exploring possible
194 sensitivities rather than as the final word on the impact of lateral mixing. The impact of changing
195 A_{Redi} on hydrographic properties is reported in Pradal and Gnanadesikan (2014), Gnanadesikan
196 et al. (2015a), Gnanadesikan et al. (2015b) and Bahl et al. (2019).

197 Modern values of oceanic temperature and salinity are used to initialize the simulations. A
198 simulation with greenhouse gases and aerosols held at 1860 values was spun up for 1500 years
199 with $A_{Redi} = 800 \text{ m}^2 \text{ s}^{-1}$. After 1500 years, five simulations are branched off this trunk run with
200 different mixing coefficients. All six simulations are then run for 1000 years. In each of the five
201 branches, the majority of the surface temperature change occurred in the first 50 years. The last
202 century, years 900 to 1000, was used to establish the climate in each case. The differences between
203 the centennially averaged ACC transports across the different runs are larger than the $\pm 2 \text{ Sv}$ range
204 in centennially smoothed transport within the control simulation. However, it is by no means clear
205 that the final state associated with equilibration of the deep ocean has been reached. The results
206 should thus be taken as indicative of the variance in ACC that can be induced by uncertainty about
207 what value of A_{Redi} to prescribe.

208 The parameterization of advective subgridscale mesoscale eddy transport is represented using a
209 spatially varying coefficient A_{GM} with a minimum coefficient of $200 \text{ m}^2 \text{ s}^{-1}$, and a maximum of
210 $1400 \text{ m}^2 \text{ s}^{-1}$. A_{GM} is computed from the local vertical shear of the horizontal velocity and width of
211 the baroclinic zone (Gnanadesikan et al. 2006) following earlier work by Griffies (1998). Insofar
212 as A_{Redi} causes changes in the stratification it also induces variation of the value of A_{GM} . As in Gal-
213 braith et al. (2011) the effective maximum slope used to compute the overturning streamfunction
214 S_{max} is 0.01.

215 The model used in this study is similar to the GFDL 1° coupled model (CM2.1) but with a
216 coarser resolution so as to decrease the computational cost of spinning up long-term simulation
217 suites. Despite the coarser resolution, CM2Mc features updates over CM2.1 including improve-
218 ments to subgrid-scale mixing parameterizations in the ocean (Galbraith et al. 2011) and a higher
219 value of S_{max} . There are physics in the ACC which are not included in this model, but as this
220 paper explores eddy parameterizations in climate models, the coarse resolution of CM2Mc suits

221 the purposes of this study. Higher resolution models can resolve eddies and might show less of an
222 impact on eastward transport due to eddy saturation effects. While our results might differ from
223 higher resolution models and the real ocean, the phenomena in CM2Mc are consistent with other
224 climate models, such as those included in CMIP5.

225 **3. Results**

226 The transport through the Drake Passage in this study's model simulations is consistent with
227 observations and with the transports of CMIP5 models. Considering the observational estimate of
228 ACC transport through the Drake Passage of 173.3 ± 10.7 Sv (Donohue et al. 2016), AREDI400,
229 AREDI800 and ABER2D fall within 2σ of the observations with respective Drake Passage trans-
230 ports of 169.7, 161.0, and 158.5 Sv, the criteria employed by Beadling et al. (2019) of assessing
231 CMIP5 models as accurate. The AREDI1200, AREDI2400, and ABERZONAL runs all lie just
232 below the observational range of uncertainty by no more than 6 Sv (Table 1). Furthermore, the
233 zonal mean wind stress produced by the models in this study compare well with the ERA-Interim
234 atmospheric reanalysis (Dee et al. 2011) and the NCEP reanalysis (Kistler et al. 2001) as well as
235 within the range of CMIP5 models (Beadling et al. 2019).

236 In order to understand these cross-model differences we first examine the changes in surface
237 wind, temperature, and salinity that arise from altering the A_{Redi} coefficient. Fig. 3 shows a
238 contour map of differences in surface properties between AREDI2400 and AREDI400. Surface
239 wind stress (top) shows both a weakening over latitudes of $45^\circ\text{S} - 65^\circ\text{S}$ and a strengthening over
240 latitudes of $30^\circ\text{S} - 45^\circ\text{S}$. This is a signature of both a weakening in the peak winds and a small
241 equatorward shift. Maximum decreases in surface wind stress reach 0.02 N m^{-2} , which amounts
242 to a 10% change with respect to the relatively realistic peak values (Seviour et al. 2017) between
243 the low and the high mixing cases. Sea surface temperature (middle panel of Fig. 3) increases

244 as A_{Redi} increases over almost the entire ocean (the exceptions being a few small regions, one off
245 the east coast of New Zealand, one in the middle of the South Atlantic at about 40°S , and one
246 off the coast of South Africa). The greatest temperature difference is an increase of about 4°C
247 west of the Drake Passage and just off the ice shelf. As this warming reduces the equator-to-pole
248 temperature gradient, it is broadly consistent with the warming driving the change in wind stress,
249 though these changes are considerably more zonal in character. Increasing lateral eddy mixing
250 generally increases salinity, but causes a small decrease in a region within the Ross Sea (bottom
251 panel of Fig. 3). As described by Pradal and Gnanadesikan (2014), the increase in salinity and
252 temperature as mixing increases can be understood in terms of additional transport of salt along
253 isopycnals destabilizing the wintertime thermocline and allowing more upward mixing of heat in
254 polar regions.

255 Fig. 4a shows the quasi-streamfunction for the low mixing case (AREDI400) relative to the
256 Southern tip of South America (so that the value at the tip of the Antarctic peninsula represents
257 the transport through Drake Passage). Note that the term quasi-streamfunction accounts for the
258 fact that there exist surface freshwater fluxes that cause a relatively small amount of divergence,
259 which is ignored to compute the streamfunction. With a transport of 169.7 Sv, this simulation is
260 within the range reported by the CMIP5 model suite of 155 ± 51 Sv as well as the Donohue et al.
261 (2016) estimate of 173.3 ± 10.7 Sv. The other plots in Fig. 4 show the differences between the
262 zonal transport in other mixing cases and the low mixing case.

263 In general, higher mixing coefficients produce lower transports in Drake Passage and in the
264 zonal mean, though the differences between AREDI2400 and AREDI1200 are relatively small.
265 As shown in Table 1, increasing A_{Redi} from 400 to 2400 reduces the transport in Drake Passage
266 by 24 Sv (about 14%) and reduces the average eastward transport across all longitudes by 37
267 Sv (about 20%). The altimetry-based estimates of mixing produce results that lie between the

268 AREDI400 and AREDI2400 cases. Note that the ABERZONAL simulation shows much larger
269 changes in ACC transports than does the ABER2D case, with a drop that is almost twice as large
270 at Drake Passage. This suggests that the full 2-D structure of the mixing in ABER2D plays an
271 important role in determining the response of the Southern Ocean, possibly because high mixing
272 coefficients are displaced away from frontal zones.

273 In all cases, the transport anomaly relative to AREDI400 is negative south of 55° S, indicating
274 counter clockwise circulation. This suggests that increasing A_{Redi} corresponds to a slowdown in
275 the component of the eastward flow associated with the subpolar gyre. Moreover, in some places,
276 like the central South Pacific and east of the Drake Passage, the negative transport anomaly extends
277 northward to about 50° S. The transport anomaly relative to AREDI400 is positive north of 55°
278 S, suggesting a shift between transport being carried in the ACC and in the subtropical gyres. In
279 the Southern Pacific, Fig. 4 shows a slowdown of the subtropical gyre while in the Atlantic and
280 Indian basins, Fig. 4 shows a northward shift in the eastward transport. In each mixing case, the
281 largest decreases in eastward transport in the Southern Ocean occur before the current enters the
282 Drake Passage at about 120° W, where the Ross Sea gyre also decreases in strength. Relative to
283 AREDI400, AREDI800 shows a decrease of 8.7 Sv in Drake Passage, but more than 24 Sv in the
284 central Ross Sea (and 13.5 Sv in the zonal average). The changes are generally smaller in the
285 Drake Passage than at other locations in the Antarctic. This indicates that the Drake Passage is
286 not a reliable indicator of significant changes in the averaged eastward volume transport in the
287 Southern Ocean as whole.

288 *a. Momentum and its balances within the Southern Ocean*

289 Because the flow through Drake Passage may not be fully representative of the whole Southern
290 Ocean, we instead examine the zonal means of transport and wind stress. As shown in Fig. 5, the

291 higher the lateral mixing parameter A_{Redi} , the lower the transport and zonal wind stress. Relative
292 to AREDI400, zonally and depth-averaged velocities (Fig. 6a) in AREDI2400 decrease by around
293 30% in Drake Passage latitudes and by around 20% north of that. By contrast, the wind stress
294 (Fig. 5c) varies much less. Peak wind stress (at 51°S) drops from 0.128 Pa to 0.114 Pa, an 11%
295 decrease, similar to the change in average wind stress from 65°S - 45°S (the region in which winds
296 decline). The changes in zonal mean velocity (Fig. 6b) look superficially similar to the changes
297 in wind stress (Fig. 6d) with larger peak anomalies in one corresponding to larger peak anomalies
298 in the other. However, it is noteworthy that even though eastward winds decrease throughout the
299 Southern Ocean, the current response in the Ross Sea is in the reverse direction as the winds
300 (which show a westward acceleration in this latitude band).

301 While larger drops in wind are associated with larger changes in the current, it seems clear that
302 theories in which the ACC transport is simply proportional to the wind stress (such that doubling
303 the wind stress leads to doubling the transport (i.e Wang (1994); Marshall (2003))) cannot explain
304 such a disproportionate response. Such linear theories fall short of describing the response of the
305 ACC to changes in wind stress. The fractional change in transport is smaller in magnitude than
306 the fractional change in wind due to compensation from eddies (Langlais et al. 2015).

307 If eddy compensation is to explain why the fractional change in transport is *greater* than the
308 fractional change in wind, A_{GM} would have to increase as A_{Redi} increased (Gent et al. 2001).
309 Instead (as shown in Fig. 6) the A_{GM} coefficients get smaller as the mixing coefficients increase,
310 with a larger drop for AREDI1200 and AREDI2400 (Fig. 6c and d) than for AREDI800 (Fig.
311 6b). The maximum parameterized eddy overturning with the Southern Ocean also drops, falling
312 from -20.5 Sv in AREDI400 to -14.7 Sv in AREDI1200 (with similar values found for ABER2D
313 and ABERZONAL, surprisingly AREDI2400 has a larger eddy overturning of -18 Sv). Both the
314 changes in A_{GM} and eddy-driven overturning are in the wrong direction to explain the modeled

315 changes in ACC transport, as less momentum is pumped out of the surface layer into the deep
316 layer by eddies as A_{Redi} increases.

317 Before further examining the impacts of the change in wind stress, we examine the mechanisms
318 behind such changes. The black line in Fig. 7a shows the difference in downward flux of eastward
319 momentum between the AREDI2400 and AREDI400 simulations. As seen by looking at the red
320 line in Fig. 7a, differences in the divergence of the column-integrated atmospheric poleward eddy
321 flux of zonal momentum largely explains these differences in surface stress (especially over the
322 Southern Ocean where topographic form stress is zero).

323 The question is then, what accounts for the changes in eddy momentum flux? As shown in Fig.
324 7b, there is a basic relationship between the upper-atmosphere (200 mb) geopotential height gra-
325 dient across the Southern Ocean (40°S - 65°S) and the poleward eddy zonal momentum flux into
326 the Southern Ocean (at 45°S) integrated across all pressure levels. A larger drop in geopotential
327 and thus a stronger atmospheric jet corresponds to a greater poleward eddy zonal momentum flux
328 at 40°S. This relationship explains both the interannual variability seen in the model and the dif-
329 ference between the two models. The blue and black point clouds in Fig. 7b are offset, indicating
330 that the AREDI2400 model never experiences the strongest gradients in zonal mean geopotential
331 height seen in AREDI400, and as a result the mean geopotential height difference between 40°S
332 and 65°S is 37 m (around 5%) lower. Despite the relatively coarse resolution of the model, the
333 relationship between eddy momentum flux and geopotential height gradient is consistent with that
334 seen in the ERA-Interim reanalysis (dashed line shows the mean slope and range over the period
335 from 1979-2010). In Fig. 7b, the point clouds have a wider spread than the dashed line, but the
336 slopes are similar. This signifies that our model shows more variability than the ERA-Interim re-
337 analysis (possibly because the 200 years shown here allow for us to see the impacts of interdecadal

338 variability which may be damped in the ECMWF record), but that the marginal sensitivity between
339 the overall change in upper layer winds and eddy momentum flux is reasonable.

340 The difference in 200 mb geopotential height, ϕ_{200} , between the AREDI2400 and AREDI400
341 simulation (Fig. 7c) is dominated by a rise over Antarctica. Warmer atmospheric temperatures
342 at pressures greater than 200 mb drives the increase in ϕ_{200} over the globe. The increase in ϕ_{200}
343 is smallest at latitudes around 40°S, where atmospheric temperatures change very little between
344 AREDI2400 and AREDI400. Poleward of this latitude, changes in the temperature of up to 2°C
345 are seen when averaged over the entire troposphere. Such changes are quite sufficient to produce
346 the tens of meters of change in ϕ_{200} . Higher temperatures over Antarctica act to decrease the
347 geopotential height gradient. This causes a smaller amount of convergence of momentum into the
348 region of maximum wind speed and results in lower wind stress at the sea surface (Starr 1948).

349 *b. Thermal Wind Shear and Buoyancy*

350 As noted above the impact of winds on ACC transport can be indirect, as the winds affect water
351 mass transformation and change the density contrast across the ACC, in turn changing the thermal
352 wind shear. We computed the differences in eastward thermal wind shear from the differences
353 in the density field at each longitude and integrate it vertically to get the velocity relative to a
354 depth of 4500 m. As shown in Fig. 8, the resulting prediction of the velocity change across the
355 ACC between AREDI2400 and AREDI400 (Fig. 8b) looks similar to the actual change (Fig. 8a).
356 Similar results have been found for other pairwise comparisons between our simulations but are
357 not shown here. This suggests (consistent with the recent results of Beadling et al. (2019)) that
358 we should focus on the density changes across the model suite rather than on bottom pressure
359 gradients and barotropic transport as the primary explanation for the differences in ACC transport.

360 Cross sections of the differences in potential temperature, salinity, and in-situ potential density
 361 between AREDI2400 and AREDI400 are shown in Fig. 9. The left-hand column shows values
 362 north of the ACC channel at 40°S and the right-hand column shows values south of the channel
 363 at 65°S. North of the channel, there is a temperature increase at the surface above about 500 m of
 364 depth of about 1°C. Below that, the temperature decreases with maximum temperature decrease
 365 of about 2°C with increasing A_{Redi} . The change in salinity is similar, with a 0.5 psu increase at the
 366 surface above around 1500 m of depth. Below that, the salinity decreases by about 0.3 psu. This
 367 results in an increase in density throughout the entire depth of the cross section of about 0.2 kg
 368 m^{-3} .

369 On the southern side of the channel, a similar pattern emerges with temperature and salinity
 370 increases at the surface and decreases at depth. The temperature increases by about 1°C at the
 371 surface, but this increase is confined to the top 200 m except in a small region at about 150°E
 372 where it dips down to about 500 m. The salinity increases by about 0.2 psu above 500 m except
 373 for in the same region where the depth of the isohaline surface dips to 1500 m. Here, on the
 374 southern side of the channel, the change in density is much smaller than on the northern edge of
 375 the channel. Nowhere on the southern edge of the channel does the density increase by more than
 376 0.2 kg m^{-3} .

377 While changing the mixing changes the mean density of the whole ocean, such changes are only
 378 marginally relevant for the thermal wind shear. To better focus on the relevant density changes we
 379 now look at zonal mean density anomalies relative to the zonally averaged value at the same depth
 380 at 65°S, defining:

$$\Delta \overline{\rho}_{65S} = \left[\overline{\rho(z, \phi, Model)} - \overline{\rho(z, \phi = 65S, Model)} \right] - \left[\overline{\rho(z, \phi, AREDI400)} - \overline{\rho(z, \phi = 65S, AREDI400)} \right] \quad (1)$$

381 In which $\rho(z, \phi, Model)$ is the density at a certain depth and latitude in the specific A_{Redi} model
 382 run, $\rho(z, \phi = 65S, Model)$ is the density at the same depth, at latitude $65^\circ S$, and in the same
 383 model run, $\rho(z, \phi, AREDI400)$ is the density at the same depth and latitude in AREDI400, and
 384 $\rho(z, \phi = 65S, AREDI400)$ is the density at the same depth at latitude $65^\circ S$ in AREDI400. This
 385 enables us to better compare density changes between simulations on a single plot without having
 386 to visually correct for different offsets in density.

387 Profiles of $\Delta\overline{\rho_{65S}}$ for each model simulation and observations are shown in Fig. 10a. The
 388 AREDI400 case is closest to observations, and the density difference across the current decreases
 389 as A_{Redi} increases. There seem to be greater changes in $\Delta\overline{\rho_{65S}}$ above 1000 m with changing A_{Redi} .
 390 The raw density differences between AREDI400 and AREDI2400 are shown in Fig. 10c. Consis-
 391 tent with Fig. 9c, the changes within the Southern Ocean are small. The relative densification of
 392 the mode and intermediate waters is a far larger signal. Additionally, increasing A_{Redi} results in a
 393 tongue of slightly denser water penetrating below 2000 m.

394 The zonal transport M_x relative to the bottom can be found by double-integrating the equation
 395 for shear relative to a motionless bottom velocity with the following equation:

$$M_x = \int_{z=-D}^0 v(z, y) \int_{y=\phi_s}^{\phi_n} dy dz = \int_{z=-D}^0 \int_{z'=-D}^z \int_{y=\phi_s}^{\phi_n} \frac{\partial v}{\partial z'} dy dz' dz \quad (2)$$

396 where v is meridional velocity, z' is the vertical coordinate (positive upward), ϕ_s is the latitude
 397 on the southern side of the ACC and ϕ_n is the latitude on the northern side of the ACC. Note that
 398 following Beadling et al. (2019) we perform this integration relative to 4500 m. Since we integrate
 399 upwards from the bottom, changes in thermal wind shear at depth will have a much larger impact
 400 on the total transport than changes near the surface (as the impact of shear on transport represents
 401 a double integration). If we only consider the component of the shear that is due to thermal wind,

402 equation 2 becomes:

$$\begin{aligned}
 M_x &\approx \frac{g}{f(55S)} \int_{z=-D}^0 \int_{z'=-D}^{z'} (\rho(45S, z') - \rho(65S, z')) dz' dz \\
 &= \frac{g}{f(55S)} \int_{z=-D}^0 (\rho(45S, z) - \rho(65S, z)) z dz \quad (3)
 \end{aligned}$$

403 where g is the acceleration due to gravity, $f(55S)$ is the Coriolis parameter at 55°S , and ρ is
 404 density. Equation 3 shows that changes in density at depth have a greater impact on transport
 405 than changes at the surface. When we multiply the density change in Fig. 10a and Fig. 10c by
 406 the depth (allowing us to properly compare the impact of density changes on transport), we get
 407 the profiles in Fig. 10b and the section in Fig. 10d, respectively. Fig. 10b shows a relatively
 408 constant impact of the cross-channel density differences below 1000 m on the thermal wind shear,
 409 though there is decrease in the impact of the shear at about 2000 m Fig. 10d shows the difference
 410 between the AREDI2400 and AREDI400 models, which highlights two regions of dynamically
 411 important density change, centered at around 1000 and 3000 m, that contribute roughly equivalent
 412 increments to the total transport.

413 These differences are not easily explained in terms of changes in surface fluxes. The surface
 414 buoyancy flux Q_{buoy} is computed as

$$Q_{buoy} = -g(\alpha Q/c_p - \beta_s F_w S) \quad (4)$$

415 where α is the coefficient of thermal expansion, Q is the surface heat flux, c_p is the specific heat of
 416 seawater, β_s is the haline contraction coefficient, F_w is the surface freshwater flux in kg s^{-1} and S
 417 is the surface salinity. As shown in Fig. 10e, the changes in the surface buoyancy flux are relatively
 418 small. There is a little more buoyancy gain between 65°S and 55°S and a little less loss north of
 419 these latitudes in AREDI400 as compared to the other model runs, but the other runs do not show
 420 much contrast from each other. We can integrate these fluxes with longitude and cumulatively

421 integrate them with longitude to get the meridional buoyancy transport needed to balance them,
422 as shown in Fig. 10f. All the models show that the Southern Ocean is a region of buoyancy gain
423 and export to lower latitudes. However, the magnitude of buoyancy export is essentially identical
424 across the simulations, although the latitude of the maximum shifts equatorward (along with the
425 peak in wind stress) as A_{Redi} increases. It is not obvious how this could explain why we see larger
426 increases in density (decrease in buoyancy) to the north of the Drake Passage latitudes than within
427 them. This suggests that we may need to look more carefully at why watermass properties appear
428 to shift across the models.

429 *c. Watermasses*

430 We examine differences in water masses by looking at changes in salinity between the
431 AREDI2400 and AREDI400 simulations in the 500-1500 m and 2000-3000 m depth bands that,
432 as seen in Fig. 10d, have a big impact on thermal wind shear (Fig. 11). The intermediate waters
433 (left column, Fig. 11) show large changes in salinity emanating from the North Pacific, which
434 propagate into the Southern Hemisphere. There is a salinification of intermediate waters in the Pa-
435 cific Basin in AREDI2400 as compared to AREDI400, which can be seen in Fig. 11c. This causes
436 densification north of the ACC at about 40°S. We interpret these changes as arising from the de-
437 stratification of the North Pacific, which strengthens the circulation in the Pacific Basin. Increasing
438 mixing tends to decrease stratification in the North Pacific as surface waters increase in salinity,
439 reducing the difference in salinity across the winter halocline (Pradal and Gnanadesikan 2014;
440 Gnanadesikan et al. 2015a; Bahl et al. 2019). Vertical exchange in the North Pacific is strongly
441 dependent on the magnitude of this salinity contrast (Gnanadesikan et al. 2015a; Bahl et al. 2019)
442 and its reduction leads to increased overturning in the Pacific Basin (Gnanadesikan et al. 2015b)).

443 The overturning circulation draws salty subtropical waters into the Northeast Pacific and shallows
444 the pycnocline throughout the global ocean.

445 By contrast, at depth, the biggest changes in salinity are seen within the Southern Ocean. As
446 A_{Redi} increases, temperature and salinity decrease at depth in the Southern Ocean. We quantify
447 this by examining T-S plots between 2000 m and 4000 m in these two simulations, shown in
448 Fig. 12. Black symbols indicate the water mass properties between 60°S and the equator, while
449 contours show the potential density referenced to 3000 m. The red stars indicate the average wa-
450 termass properties at 40°S. In the AREDI400 case, the mean watermass properties at this latitude
451 ($T = 3.5^{\circ}\text{C}$, $S = 34.83$ psu) are close to the midpoint between Antarctic and North Atlantic water
452 masses. A quantitative watermass analysis shows that at this latitude, 49% of the water is of North
453 Atlantic origin ($T = 5^{\circ}\text{C}$, $S = 35.12$ psu), 21% is Circumpolar Deep Water from the deep Southern
454 Ocean ($T = 0.5^{\circ}\text{C}$, $S = 34.6$ psu) and the remaining 30% is from the intermediate water classes
455 ($T = 3^{\circ}\text{C}$, $S = 34.6$ psu). In the AREDI2400 case, by contrast, the mean temperature and salinity
456 ($T = 1.98^{\circ}\text{C}$, $S = 34.66$ psu) lie much closer to the intermediate water end member ($T = 2^{\circ}\text{C}$,
457 $S = 34.53$ psu), suggesting that only 22% of the water at 40°S is of North Atlantic ($T = 4.5^{\circ}\text{C}$,
458 $S = 35.15$ psu) origin, 29% is Circumpolar Deep Water and 49% is intermediate water. Increas-
459 ing A_{Redi} leads to a decrease in North Atlantic water but an increase in Circumpolar Deep water
460 and intermediate water. As there is no deep water formation at these latitudes, we interpret these
461 changes as a northward shift in the front between fresher but denser Antarctic Bottom Water and
462 saltier but lighter North Atlantic Deep water. It appears that when A_{Redi} is larger, Antarctic water
463 more readily escapes the Southern Ocean, reducing the deep cross-ACC density gradients and thus
464 the transport.

465 What accounts for the shift in the deep front? As shown in Fig. 13a, the region of increased
466 density in AREDI2400 lies immediately below a region where the wind stress curl increases.

467 Because the wind stress curl in this region is negative, this change makes the region less favorable
468 to downwelling. A hypothesis, then, is that the change in wind stress curl propagates all the
469 way to the bottom because the mean currents in this region (black line, Fig. 13b) are faster than
470 the baroclinic Rossby wave speed $c = \beta L_R^2$ (red line, Fig. 13b). This means that the baroclinic
471 concentration of momentum near the surface described by Gill (1982) is unable to hold. Currents
472 which flow much faster than the baroclinic Rossby wave speed display an equivalent-barotropic
473 structure and as such the flow at depth is closely related to the surface flow (see also Hughes (2005)
474 for more discussion of this mechanism).

475 **4. Conclusions**

476 In this study, we observed dynamical changes that arose in the circulation in the Southern Ocean
477 due to variations in the lateral eddy mixing. Our results demonstrate that in a coupled climate
478 model, increasing the value of A_{Redi} acts in the same general sense as increasing the value of
479 A_{GM} . Both parameters should be taken into account as important to the circulation in the South-
480 ern Ocean. Using a coupled model helps to illuminate the multifaceted relationships between
481 mixing, sea surface temperatures, winds, and subsurface density structure. In contrast to model
482 studies such as Gnanadesikan and Hallberg (2000) where surface densities were fixed to observa-
483 tions, coupled models allow for changes in winds, SSTs and subsurface density to be dynamically
484 consistent.

485 Increasing A_{Redi} resulted in a notable slowing of the transport of the ACC. However, the greatest
486 changes in transport occur outside of the Drake Passage, suggesting that modelers may need to
487 consider a wider range of diagnostics than just the transport within the passage when assessing the
488 representation of the ACC in models. The relative change in transport was about 2.5 times greater
489 in magnitude than the relative change in wind stress, suggesting that simple models that predict

490 that the transport is directly proportional to wind stress (Wang 1994) or wind stress curl (Warren
491 et al. 1996) are unlikely to be correct. The changes in transport in the Southern Ocean were caused
492 by alterations to the density structure to the north of the ACC channel, although naively we would
493 not expect varying A_{Redi} to produce such a change. An increase in density in intermediate and deep
494 waters on the northern edge of the ACC appears to explain the change in transport. By destratifying
495 the North Pacific and increasing northern overturning (Gnanadesikan et al. 2015a; Bahl et al.
496 2019), increasing A_{Redi} shallows the pycnocline and increases the density of intermediate waters
497 to the north of the ACC. This reduces the density contrast across the ACC and thus the decreases
498 thermal wind shear in the upper half of the water column. By increasing the wind stress curl
499 within the Southern Ocean in regions where the eastward velocities are higher than the Rossby
500 wave speed, the result is to move isopycnals upward in the water column, effectively allowing
501 dense Antarctic waters to penetrate a little further to the north, contributing to the reduction of
502 density contrast in deep waters where it can have a large impact on transport. Our results support
503 both the ideas that changes in large-scale overturning can affect the ACC (following Gnanadesikan
504 and Hallberg (2000); Fučkar and Vallis (2007)) and that changes in wind stress curl may also affect
505 ACC transport (though not to the extent hypothesized by Warren et al. (1996)).

506 Although the range of ACC transports seen herein is significant, it is much smaller than the
507 range seen in the CMIP5 models (Beadling et al. 2019) as well as in Russell et al. (2006). This
508 suggests that though A_{Redi} coefficients differ greatly between models, they are unlikely to account
509 for the majority of the differences in transport. Rather, it is likely that differences in overturning in
510 the Northern hemisphere, or large differences in the structure of Southern Ocean winds (processes
511 which may be linked to each other) play the dominant role.

512 Our results also illustrate the impact of including more realistic representations of A_{Redi} in ocean
513 models. The representation of A_{Redi} developed by Abernathey and Marshall (2013) produces a

514 transport of 158 Sv, which is reasonable by the standards of CMIP3 or CMIP5, despite having
515 A_{Redi} coefficients which exceed $10,000 \text{ m}^2 \text{ s}^{-1}$ in some locations. From this we conclude that
516 these high values are occurring in locations where they have relatively weak impact on the density
517 structure. The full 2D structure is important - zonally averaging the diffusion coefficient produces
518 a much larger impact on transport. This may be because zonally averaging the diffusion coefficient
519 raises it in places where Abernathy and Marshall (2013) find suppression of A_{Redi} by fast moving
520 currents with larger tracer gradients. Future work will need to provide a fully three-dimensional
521 picture of how this critical parameter varies, both in space and time.

522 *Acknowledgments.* This work was supported by the National Science Foundation under NSF
523 proposal FESD-1338814. We thank Will Seviour, Jordan Thomas, Kyle Armour, Spencer Jones,
524 and Peter Gent for comments on earlier versions of this manuscript and gratefully acknowl-
525 edge computing resources provided by the Institute for Data Intensive Engineering and Science
526 (IDIES) at Johns Hopkins University. Model climatologies are provided in NetCDF format at
527 pages.jh.edu/~agnanad1/datasets.html.

528 **References**

- 529 Abernathy, R. P., and J. Marshall, 2013: Global surface eddy diffusivities derived from satellite
530 altimetry. *J. Geophys. Res.*, **118**, 901–916.
- 531 Alley, R. B., S. Anandakrishnan, K. Christianson, H. J. Horan, A. Muto, B. R. Parizek, D. Pollard,
532 and R. T. Walker, 2015: Oceanic forcing of ice-sheet retreat: West antarctica and more. *Annu.*
533 *Rev. Earth and Planetary Sciences*, **43**, 207–231, doi:10.1146/annurev-earth-060614-105344.
- 534 Alley, R. B., P. U. Clark, P. Huybrechts, and I. Joughin, 2005: Ice-sheet and sea-level changes.
535 *Science*, **310**, 456–460, doi:10.1126/science.1114613.

536 Bahl, A. A., A. Gnanadesikan, and M. A. Pradal, 2019: Variations in ocean deoxygenation across
537 earth system models: Isolating the role of parameterized lateral mixing. *Global Biogeochemical*
538 *Cycles*, **33**, 703–724, doi:10.1029/2018GB006121.

539 Beadling, R. L., J. L. Russell, R. J. Stouffer, P. J. Goodman, and M. Mazloff, 2019: Assessing
540 the quality of southern ocean circulation in cmip5 aogcm and earth system model simulations.
541 *Journal of Climate*, **32** (18), 5915–5940, doi:10.1175/JCLI-D-19-0263.1.

542 Bentsen, M., and Coauthors, 2013: The norwegian earth system model, noresm1-m-part 1: De-
543 scription and basic evaluation. *Geoscientific Model Development Discussions*, **5**, 2843–2931.

544 Caldeira, K., and P. B. Duffy, 2000: The role of the southern ocean in uptake and storage of
545 anthropogenic carbon dioxide. *Science*, **287**, 620–622.

546 Cunningham, S. A., S. Alderson, B. King, and M. Brandon, 2003: Transport and variability
547 of the antarctic circumpolar current in drake passage. *J. Geophys. Res.*, **108**, doi:10.1029/
548 2001JC001147.

549 Dee, D. P., and Coauthors, 2011: The era-interim reanalysis: configuration and performance of
550 the data assimilation system. *Quarterly Journal of the Royal Meteorological Society*, **137** (656),
551 553–597, doi:10.1002/qj.828.

552 Doddridge, E. W., J. Marshall, H. Song, J.-M. Campin, M. Kelley, and L. Nazarenko,
553 2019: Eddy compensation dampens southern ocean sea surface temperature re-
554 sponse to westerly wind trends. *Geophysical Research Letters*, **46** (8), 4365–4377,
555 doi:10.1029/2019GL082758, URL [https://agupubs.onlinelibrary.wiley.com/doi/abs/10.1029/
556 2019GL082758](https://agupubs.onlinelibrary.wiley.com/doi/abs/10.1029/2019GL082758), <https://agupubs.onlinelibrary.wiley.com/doi/pdf/10.1029/2019GL082758>.

557 Donohue, K. A., K. L. Tracey, D. R. Watts, M. P. Chidichimo, and T. K. Chereskin, 2016: Mean
558 antarctic circumpolar current transport measured in drake passage. *Geophys. Res. Letters*, **43**,
559 11 760–11 767, doi:10.1002/2016GL070319.

560 Dufour, C. O., J. L. Sommer, J. D. Zika, M. Gehlen, J. C. Orr, P. Mathiot, and B. Barnier, 2012:
561 Standing and transient eddies in the response of the southern ocean meridional overturning to
562 the southern annular mode. *J. Climate*, **25**, 6958–6974, doi:10.1175/JCLI-D-11-00309.1.

563 Dunne, J., and Coauthors, 2012: Gfds esm2 global coupled climatecarbon earth system models.
564 part i: Physical formulation and baseline simulation characteristics. *J. Climate*, **25**, 6646–6665,
565 doi:10.1175/JCLI-D-11-00560.1.

566 Farneti, R., and P. R. Gent, 2011: The effects of the eddy-induced advection coefficient in a
567 coarse-resolution coupled climate model. *Ocean Modelling*, **39** (1), 135 – 145.

568 Fogli, P., and Coauthors, 2009: Ingv-cmcc carbon (icc): A carbon cycle earth system model.
569 *CMCC Research Paper*.

570 Frölicher, T. L., J. Sarmiento, D. Paynter, J. Dunne, J. Krasting, and M. Winton, 2015: Dominance
571 of the southern ocean in anthropogenic carbon and heat uptake in cmip5 models. *J. Climate*, **28**,
572 862–886.

573 Fučkar, N. S., and G. K. Vallis, 2007: Interhemispheric influence of surface buoyancy conditions
574 on a circumpolar current. *Geophysical Research Letters*, **34** (14), doi:10.1029/2007GL030379.

575 Galbraith, E. D., and Coauthors, 2011: Climate variability and radiocarbon in the cm2mc earth
576 system model. *Journal of Climate*, **24** (16), 4230–4254, doi:10.1175/2011JCLI3919.1.

577 Gent, P. R., W. G. Large, and F. O. Bryan, 2001: What sets the mean transport through
578 drake passage? *Journal of Geophysical Research: Oceans*, **106** (C2), 2693–2712, doi:
579 10.1029/2000JC900036.

580 Gent, P. R., and J. C. McWilliams, 1990: Isopycnal mixing in ocean circulation models. *Journal of*
581 *Physical Oceanography*, **20** (1), 150–155, doi:10.1175/1520-0485(1990)020<0150:IMIOCM>
582 2.0.CO;2.

583 Giglio, D., and G. C. Johnson, 2016: Subantarctic and polar fronts of the antarctic circumpolar
584 current and southern ocean heat and freshwater content variability: A view from argo. *Journal*
585 *of Physical Oceanography*, **46** (3), 749–768, doi:10.1175/JPO-D-15-0131.1.

586 Gill, A. E., 1982: *Atmosphere Ocean Dynamics*. Academic Press.

587 Gille, S. T., 1997: The southern ocean momentum balance: Evidence for topographic effects
588 from numerical model output and altimeter data. *Journal of Physical Oceanography*, **27** (10),
589 2219–2232, doi:10.1175/1520-0485(1997)027<2219:TSOMBE>2.0.CO;2.

590 Gnanadesikan, A., 1999: A simple predictive model for the structure of the oceanic pyc-
591 nocline. *Science*, **283** (5410), 2077–2079, doi:10.1126/science.283.5410.2077, URL <https://science.sciencemag.org/content/283/5410/2077>,
592 [https://science.sciencemag.org/content/283/](https://science.sciencemag.org/content/283/5410/2077)
593 [5410/2077.full.pdf](https://science.sciencemag.org/content/283/5410/2077.full.pdf).

594 Gnanadesikan, A., D. Bianchi, and M.-A. Pradal, 2013: Critical role for mesoscale eddy diffusion
595 in supplying oxygen to hypoxic ocean waters. *Geophysical Research Letters*, **40** (19), 5194–
596 5198, doi:10.1002/grl.50998.

- 597 Gnanadesikan, A., and R. W. Hallberg, 2000: On the relationship of the circumpolar current to
598 southern hemisphere winds in coarse-resolution ocean models. *Journal of Physical Oceanogra-*
599 *phy*, **30** (8), 2013–2034, doi:10.1175/1520-0485(2000)030<2013:OTROTC>2.0.CO;2.
- 600 Gnanadesikan, A., M.-A. Pradal, and R. Abernathey, 2015a: Exploring the isopycnal mixing and
601 helium heat paradoxes in a suite of earth system models. *Ocean Science*, **11** (4), 591–605, doi:
602 10.5194/os-11-591-2015.
- 603 Gnanadesikan, A., M.-A. Pradal, and R. Abernathey, 2015b: Isopycnal mixing by mesoscale ed-
604 dies significantly impacts oceanic anthropogenic carbon uptake. *Geophysical Research Letters*,
605 **42** (11), 4249–4255, doi:10.1002/2015GL064100.
- 606 Gnanadesikan, A., and Coauthors, 2006: Gfdl’s cm2 global coupled climate models. part ii: The
607 baseline ocean simulation. *Journal of Climate*, **19** (5), 675–697, doi:10.1175/JCLI3630.1.
- 608 Griffies, S. M., 1998: The gentmcwilliams skew flux. *Journal of Physical Oceanography*, **28** (5),
609 831–841, doi:10.1175/1520-0485(1998)028<0831:TGMSF>2.0.CO;2.
- 610 Hallberg, R., and A. Gnanadesikan, 2001: An exploration of the role of transient eddies in deter-
611 mining the transport of a zonally reentrant current. *Journal of Physical Oceanography*, **31** (11),
612 3312–3330, doi:10.1175/1520-0485(2001)031<3312:AEOTRO>2.0.CO;2.
- 613 Hallberg, R., and A. Gnanadesikan, 2006: The role of eddies in determining the structure and
614 response of the wind-driven southern hemisphere overturning: Results from the modeling eddies
615 in the southern ocean (meso) project. *Journal of Physical Oceanography*, **36** (12), 2232–2252,
616 doi:10.1175/JPO2980.1.
- 617 Hughes, C. W., 2005: Nonlinear vorticity balance of the antarctic circumpolar current. *Journal of*
618 *Geophysical Research: Oceans*, **110** (C11), doi:10.1029/2004JC002753.

- 619 Ito, T., M. Woloszyn, and M. Mazloff, 2010: Anthropogenic carbon dioxide transport in the south-
620 ern ocean driven by ekman flow. *Nature*, **463**, 80–3, doi:10.1038/nature08687.
- 621 Johns, T. C., and Coauthors, 2006: The new hadley centre climate model (hadgem1): Evaluation
622 of coupled simulations. *Journal of Climate*, **19** (7), 1327–1353, doi:10.1175/JCLI3712.1.
- 623 Johnson, G. C., and H. L. Bryden, 1989: On the size of the antarctic circumpolar current. *Deep Sea*
624 *Research Part A. Oceanographic Research Papers*, **36** (1), 39 –53, doi:10.1016/0198-0149(89)
625 90017-4.
- 626 Jones, D. C., T. Ito, and N. S. Lovenduski, 2011: The transient response of the southern
627 ocean pycnocline to changing atmospheric winds. *Geophysical Research Letters*, **38** (15),
628 doi:10.1029/2011GL048145, URL [https://agupubs.onlinelibrary.wiley.com/doi/abs/10.1029/
629 2011GL048145](https://agupubs.onlinelibrary.wiley.com/doi/abs/10.1029/2011GL048145), <https://agupubs.onlinelibrary.wiley.com/doi/pdf/10.1029/2011GL048145>.
- 630 Karsten, R. H., and J. Marshall, 2002: Testing theories of the vertical stratification of the acc
631 against observations. *Dynamics of Atmospheres and Oceans*, **36**, 233–246.
- 632 Kistler, R., and Coauthors, 2001: The ncepncar 50-year reanalysis: Monthly means cd-rom and
633 documentation. *Bulletin of the American Meteorological Society*, **82** (2), 247–268, doi:10.1175/
634 1520-0477(2001)082<0247:TNNYRM>2.3.CO;2.
- 635 Langlais, C. E., S. R. Rintoul, and J. D. Zika, 2015: Sensitivity of antarctic circumpolar current
636 transport and eddy activity to wind patterns in the southern ocean. *Journal of Physical Oceanog-*
637 *raphy*, **45** (4), 1051–1067, doi:10.1175/JPO-D-14-0053.1.
- 638 Ledwell, J. R., A. J. Watson, and C. S. Law, 1998: Mixing of a tracer in the pycnocline. *Journal*
639 *of Geophysical Research: Oceans*, **103** (C10), 21 499–21 529, doi:10.1029/98JC01738, URL
640 <https://agupubs.onlinelibrary.wiley.com/doi/abs/10.1029/98JC01738>.

- 641 Lumpkin, R., and P. Flament, 2001: Lagrangian statistics in the central north pacific. *Journal of*
642 *Marine Systems*, **29**, 141–155, doi:10.1016/S0924-7963(01)00014-8.
- 643 Marshall, G. J., 2003: Trends in the southern annular mode from observations and reanalyses.
644 *Journal of Climate*, **16 (24)**, 4134–4143, doi:10.1175/1520-0442(2003)016<4134:TITSAM>2.
645 0.CO;2.
- 646 Meijers, A. J. S., 2014: The southern ocean in the coupled model intercomparison project phase
647 *5. Philosophical transactions. Series A, Mathematical, physical, and engineering sciences*, **372**,
648 doi:10.1098/rsta.2013.0296.
- 649 Meijers, A. J. S., E. Shuckburgh, N. Bruneau, J.-B. Sallee, T. J. Bracegirdle, and Z. Wang, 2012:
650 Representation of the antarctic circumpolar current in the cmip5 climate models and future
651 changes under warming scenarios. *Journal of Geophysical Research: Oceans*, **117 (C12)**, doi:
652 10.1029/2012JC008412.
- 653 Meredith, M. P., and A. M. Hogg, 2006: Circumpolar response of southern ocean eddy ac-
654 tivity to a change in the southern annular mode. *Geophysical Research Letters*, **33 (16)**,
655 doi:10.1029/2006GL026499, URL [https://agupubs.onlinelibrary.wiley.com/doi/abs/10.1029/](https://agupubs.onlinelibrary.wiley.com/doi/abs/10.1029/2006GL026499)
656 [2006GL026499](https://agupubs.onlinelibrary.wiley.com/doi/pdf/10.1029/2006GL026499), <https://agupubs.onlinelibrary.wiley.com/doi/pdf/10.1029/2006GL026499>.
- 657 Morrison, A. K., and A. McC. Hogg, 2013: On the relationship between southern ocean over-
658 turning and acc transport. *Journal of Physical Oceanography*, **43 (1)**, 140–148, doi:10.1175/
659 JPO-D-12-057.1.
- 660 Munday, D. R., H. L. Johnson, and D. P. Marshall, 2013: Eddy saturation of equilibrated circumpolar
661 lar currents. *Journal of Physical Oceanography*, **43 (3)**, 507–532, doi:10.1175/JPO-D-12-095.1.

662 Munk, W. H., and E. Palmén, 1951: Note on the dynamics of the antarctic circumpolar current1.
663 *Tellus*, **3** (1), 53–55, doi:10.1111/j.2153-3490.1951.tb00776.x, URL <https://onlinelibrary.wiley.com/doi/abs/10.1111/j.2153-3490.1951.tb00776.x>, <https://onlinelibrary.wiley.com/doi/pdf/10.1111/j.2153-3490.1951.tb00776.x>.
664
665

666 Naveira Garabato, A. C., K. L. Polzin, R. Ferrari, J. D. Zika, and A. Forryan, 2016: A microscale
667 view of mixing and overturning across the antarctic circumpolar current. *Journal of Physical*
668 *Oceanography*, **46** (1), 233–254, doi:10.1175/JPO-D-15-0025.1.

669 Pradal, M.-A., and A. Gnanadesikan, 2014: How does the redi parameter for mesoscale mixing
670 impact global climate in an earth system model? *Journal of Advances in Modeling Earth Sys-*
671 *tems*, **6** (3), 586–601, doi:10.1002/2013MS000273.

672 Pritchard, H., S. Ligtenberg, H. Fricker, D. Vaughan, M. Van den Broeke, and L. Padman, 2012:
673 Antarctic ice-sheet loss driven by basal melting of ice shelves. *Nature*, **484**, 502–5, doi:10.1038/
674 nature10968.

675 Redi, M. H., 1982: Oceanic isopycnal mixing by coordinate rotation. *Journal of Physical*
676 *Oceanography*, **12** (10), 1154–1158, doi:10.1175/1520-0485(1982)012<1154:OIMBCR>2.0.
677 CO;2.

678 Rintoul, S., 2009: Antarctic circumpolar current. *Encyclopedia of the Antarctic*, 178–190, doi:
679 10.1016/B978-012374473-9.00603-2.

680 Russell, J. L., R. J. Stouffer, and K. W. Dixon, 2006: Intercomparison of the southern ocean
681 circulations in ipcc coupled model control simulations. *Journal of Climate*, **19** (18), 4560–4575,
682 doi:10.1175/JCLI3869.1.

- 683 Seviour, W. J. M., A. Gnanadesikan, D. Waugh, and M.-A. Pradal, 2017: Transient response of
684 the southern ocean to changing ozone: Regional responses and physical mechanisms. *Journal*
685 *of Climate*, **30** (7), 2463–2480, doi:10.1175/JCLI-D-16-0474.1.
- 686 Starr, V. P., 1948: An essay on the general circulation of the earth's atmosphere. *Journal of Mete-*
687 *orology*, **5** (2), 39–43.
- 688 Straub, D. N., 1993: On the transport and angular momentum balance of channel models of the
689 antarctic circumpolar current. *Journal of Physical Oceanography*, **23** (4), 776–782, doi:10.1175/
690 1520-0485(1993)023<0776:OTTAAM>2.0.CO;2.
- 691 Tansley, C. E., and D. P. Marshall, 2001: On the dynamics of wind-driven circumpolar cur-
692 rents. *Journal of Physical Oceanography*, **31** (11), 3258–3273, doi:10.1175/1520-0485(2001)
693 031<3258:OTDOWD>2.0.CO;2.
- 694 Wang, L., 1994: A linear homogeneous model for topographic control of the antarctic circumpolar
695 current. *Journal of Marine Research*, **52** (4), 649–685, doi:doi:10.1357/0022240943076993.
- 696 Warren, B. A., J. H. Lacasce, and P. E. Robbins, 1996: On the Obscurantist Physics of "Form
697 Drag" in Theorizing about the Circumpolar Current. *Journal of Physical Oceanography*, **26**,
698 2297–2304, doi:10.1175/1520-0485(1996)026<2297:OTOPOD>2.0.CO;2.
- 699 Whitworth, T., and R. G. Peterson, 1985: Volume transport of the antarctic circumpolar current
700 from bottom pressure measurements. *Journal of Physical Oceanography*, **15** (6), 810–816.
- 701 Worthington, L., 1981: The water masses of the world ocean: Some results of a fine-scale census.
702 *Evolution of Physical Oceanography, Scientific Surveys in Honor of Henry Stommel*, W. B. A.,
703 and W. C., Eds., MIT Press, Cambridge, MA, 42–60.

704 **LIST OF TABLES**

705 **Table 1.** Averaged diagnostics across the model suite. Second column shows eastward
706 transport in Drake Passage in Sv. Third column shows the averaged eastward
707 transport in the latitude band from $40 - 65^{\circ}S$ (where as seen in Fig. 6 the zonal
708 mean velocities are eastward). Column 4 shows the mean wind stress from
709 $45 - 65^{\circ}S$, covering the region where changes are generally in the same sense. . . . 34

710 TABLE 1. Averaged diagnostics across the model suite. Second column shows eastward transport in Drake
711 Passage in Sv. Third column shows the averaged eastward transport in the latitude band from $40 - 65^\circ S$ (where
712 as seen in Fig. 6 the zonal mean velocities are eastward). Column 4 shows the mean wind stress from $45 - 65^\circ S$,
713 covering the region where changes are generally in the same sense.

Model	Drake Passage Transport (Sv)	65S-40S Transport (Sv)	Mean Wind Stress (Pa)
ARED1400	169.7	193.5	0.103
ARED1800	161.0	179.1	0.098
ARED11200	146.6	157.3	0.092
ARED12400	145.8	155.8	0.091
ABER2D	158.5	167.9	0.096
ABERZONAL	148.6	159.2	0.093

714 **LIST OF FIGURES**

715 **Fig. 1.** Schematic of eddy impacts in the ocean. Left hand side shows impact of Gent-McWilliams
716 parameterization. Right hand side shows impact of Redi along-isopycnal mixing that is the
717 focus of this manuscript. 37

718 **Fig. 2.** Mixing coefficients from Abernathey and Marshall (2013) altimetric product mapped to
719 model grid. (A) Full 2-D field, used in ABER2D simulation. (B) Zonally averaged version
720 used in ABERZONAL simulation. 38

721 **Fig. 3.** Differences between high mixing (AREDI2400) and low mixing (AREDI400) cases. (A)
722 Zonal wind stress at the air-sea interface. (B) sea surface temperature. (C) Sea surface
723 salinity. 39

724 **Fig. 4.** Plots showing zonal (east-west) transport and differences relative to the lowest constant mix-
725 ing case anomalies in Sv. (A) AREDI400 transport. (B) transport difference, AREDI800-
726 AREDI400. (C) transport difference, AREDI1200-AREDI400. (D) transport difference,
727 AREDI2400-AREDI400. (E) transport difference, ABER2D-AREDI400. (F) transport dif-
728 ference, ABERZONAL-AREDI400. 40

729 **Fig. 5.** Momentum in the Southern Ocean (A) Zonal mean velocity for all six mixing cases is shown
730 from 80°S to 20°S. (B) Zonal mean velocity difference relative to AREDI400 for the other 5
731 cases. (C) Zonal mean wind stress in Pa, NCEP observations shown by the thick black line
732 with symbols. (D) Zonal mean zonal wind stress difference relative to AREDI400 for the
733 other 5 cases. 41

734 **Fig. 6.** Gent McWilliams coefficients A_{GM} in the Southern Ocean across the model suite. (A)
735 AREDI400 simulation. (B) difference in A_{GM} AREDI800-AREDI400 (C) difference in
736 A_{GM} AREDI1200-AREDI400 (D) difference in A_{GM} AREDI2400-AREDI400 (E) differ-
737 ence in A_{GM} AREDI800-ABER2D (F) difference in A_{GM} AREDI800-ABERZONAL. 42

738 **Fig. 7.** Dynamically relevant changes in the atmosphere between AREDI2400 and AREDI400. (A)
739 Changes in momentum transport. Black line shows change in surface wind stress. Red line
740 shows change in momentum flux convergence. (B) Relationship between momentum flux at
741 40S and geopotential height difference between 40°S and 65°S. Symbols show AREDI400
742 (black) and AREDI2400 (blue). Dashed line shows equivalent range and slope of rela-
743 tionship in ERA-Interim reanalysis. (C) Change in 200 mb geopotential height, illustrating
744 increase over Antarctica. (D) Change in temperature at heights below (pressures above)
745 200 mb illustrating connection between increase in geopotential height and surface warming. 43

746 **Fig. 8.** Comparison of changes between AREDI2400 and AREDI400 case. (A) Zonal mean veloc-
747 ity. (B) Velocity change relative to 4500 m computed from thermal wind shear. 44

748 **Fig. 9.** Circumpolar cross sections of changes between AREDI2400 and AREDI400 in potential
749 temperature (top row), salinity (middle row) and in-situ density (bottom row). The left-hand
750 column shows changes at 40°S while the right-hand column shows changes at 65°S. 45

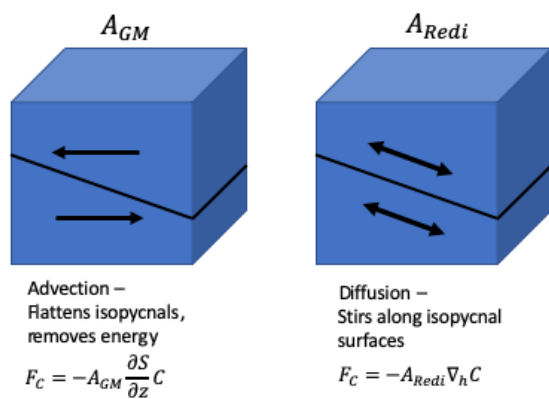
751 **Fig. 10.** (A) Profiles of zonally averaged difference in density between 45°S and 65°S for each sim-
752 ulation and observations. (B) Profiles of zonally averaged difference in density between
753 45°S and 65°S multiplied by depth, highlighting locations most important for changing
754 the baroclinic transport. (C) Zonally averaged change in density relative to 65°S between
755 AREDI2400 and AREDI400. (D) Zonally averaged change in density relative to 65°S mul-

756 tiplied by depth (E) Zonally averaged surface buoyancy flux. (F) Cumulatively integrated
757 buoyancy flux, indicating transport that would be required to balance the fluxes in (E). . . . 46

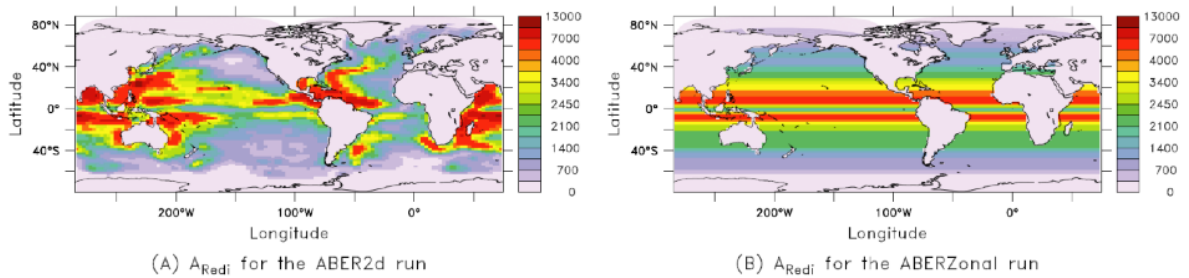
758 **Fig. 11.** Salinity fields at 500 – 1500 *m* (left column) and 2000 – 4000 *m* (right column). Top row
759 shows values for AREDI400, middle AREDI2400 and bottom the difference between the
760 two. Note that the increase in Pacific sector salinity within the Southern ocean shallower
761 depths can be tracked back to the North Pacific, while the differences at greater depth are
762 largest within the Southern Ocean. 47

763 **Fig. 12.** T-S plots for the Southern Hemisphere from 60°S to the equator in the AREDI400 model
764 (A) and AREDI2400 model (B). Contours show potential density referenced to 3000 *m*. Red
765 star shows average value at 40°S. 48

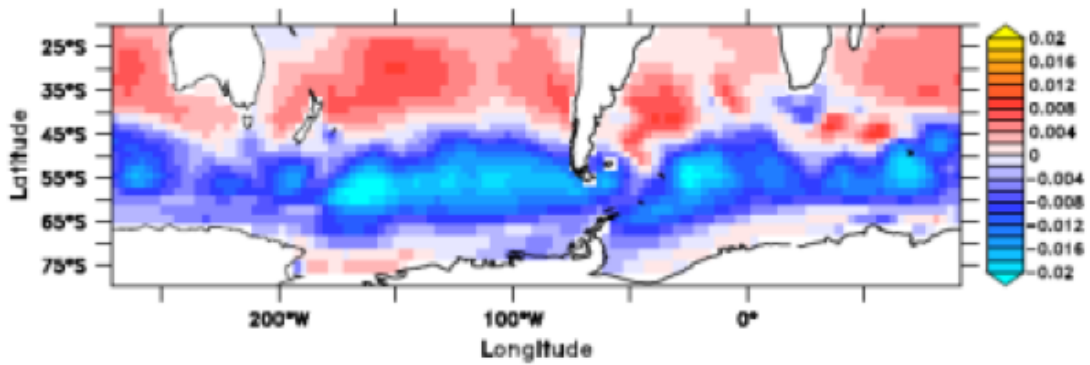
766 **Fig. 13.** Explaining deep density changes. (A) Southern hemisphere changes in density at 400 *m*
767 (colors) overlaid with contours of wind stress curl showing that the most intense changes
768 are found in latitudes with positive anomalous wind stress curl. (B) Comparison of zon-
769 ally and depth-averaged velocities (black line) and zonally averaged Rossby wave speed
770 (red line), showing that between about 65°S and 40°S the mean velocities exceed the 1st
771 baroclinic Rossby wave speed and so changes in wind stress curl would be expected to be
772 communicated to the bottom. 49



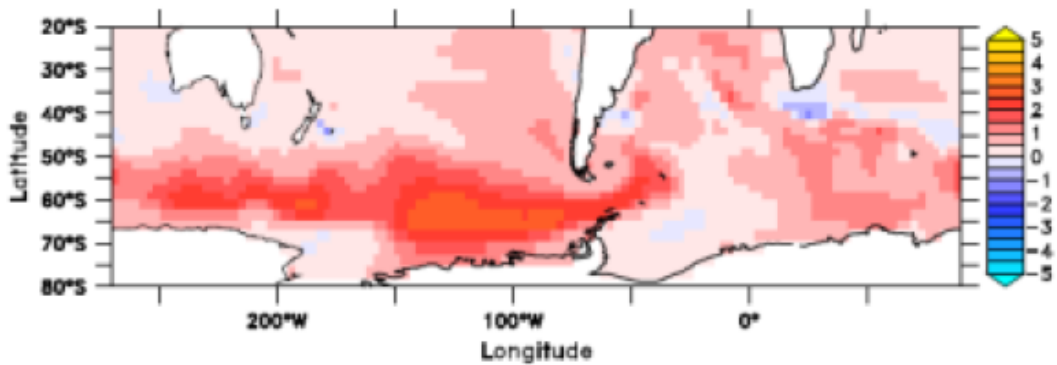
773 FIG. 1. Schematic of eddy impacts in the ocean. Left hand side shows impact of Gent-McWilliams parame-
774 terization. Right hand side shows impact of Redi along-isopycnal mixing that is the focus of this manuscript.



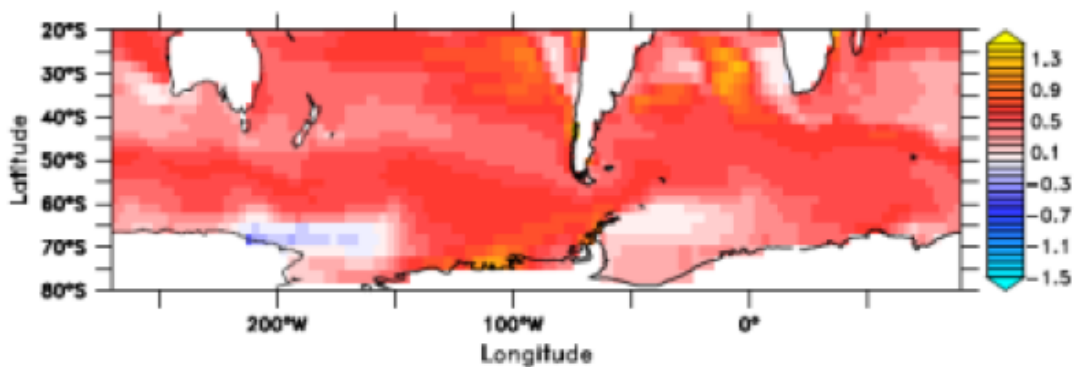
775 FIG. 2. Mixing coefficients from Abernathey and Marshall (2013) altimetric product mapped to model grid.
 776 (A) Full 2-D field, used in ABER2D simulation. (B) Zonally averaged version used in ABERZONAL simulation.



(A) Surface wind stress difference ARedi2400 – ARedi400

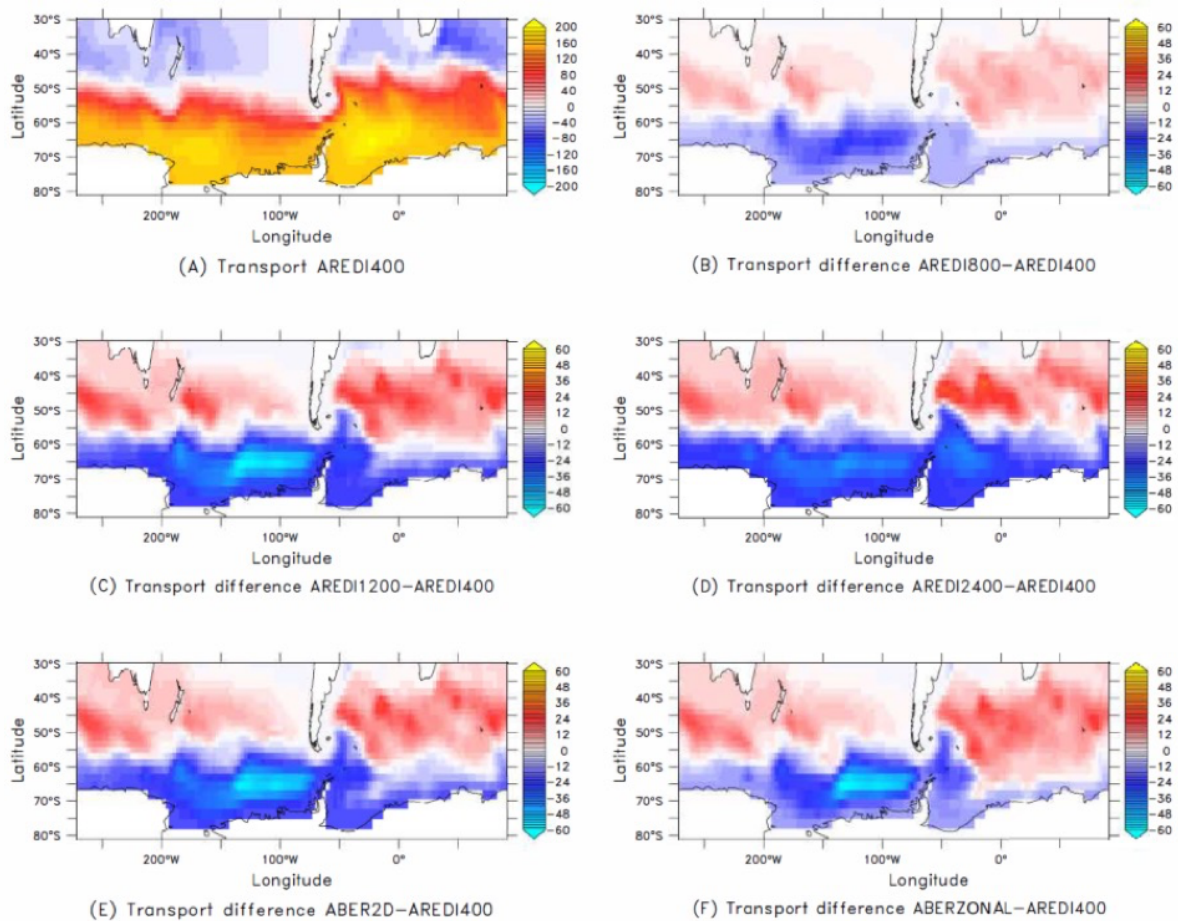


(B) SST difference ARedi2400 – ARedi400

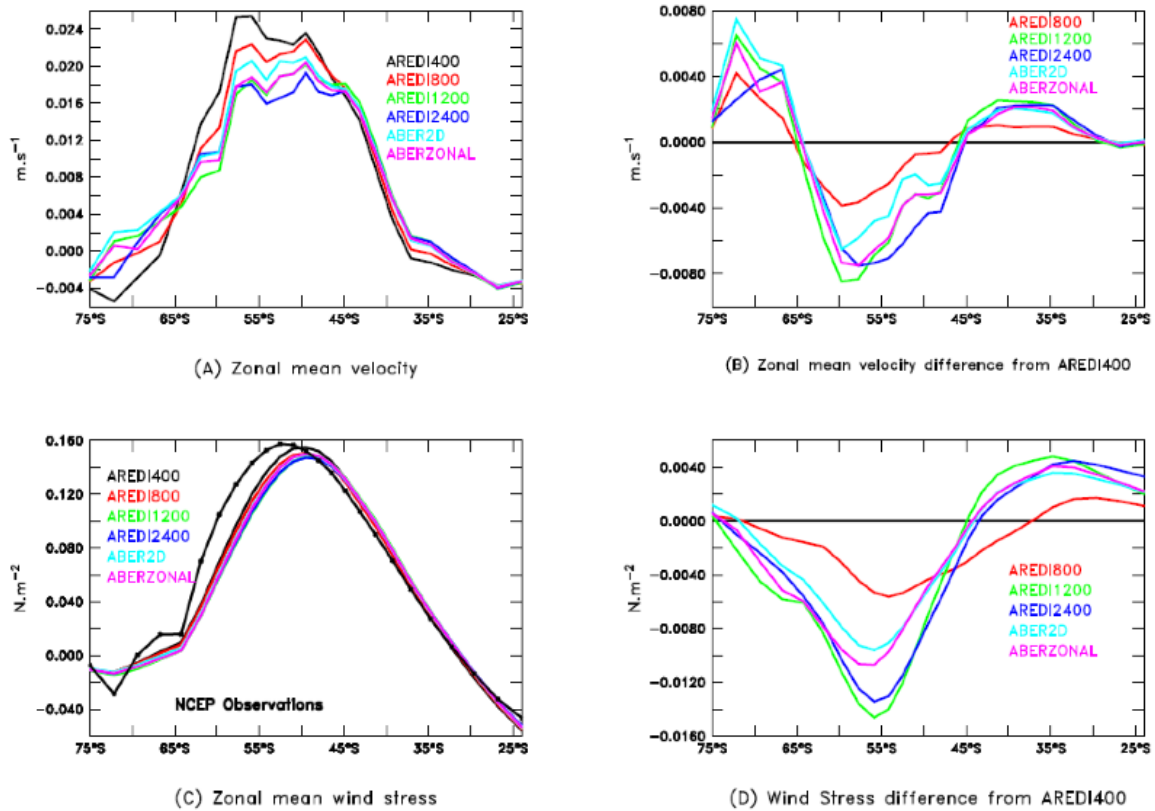


(C) SSS difference ARedi2400 – ARedi400

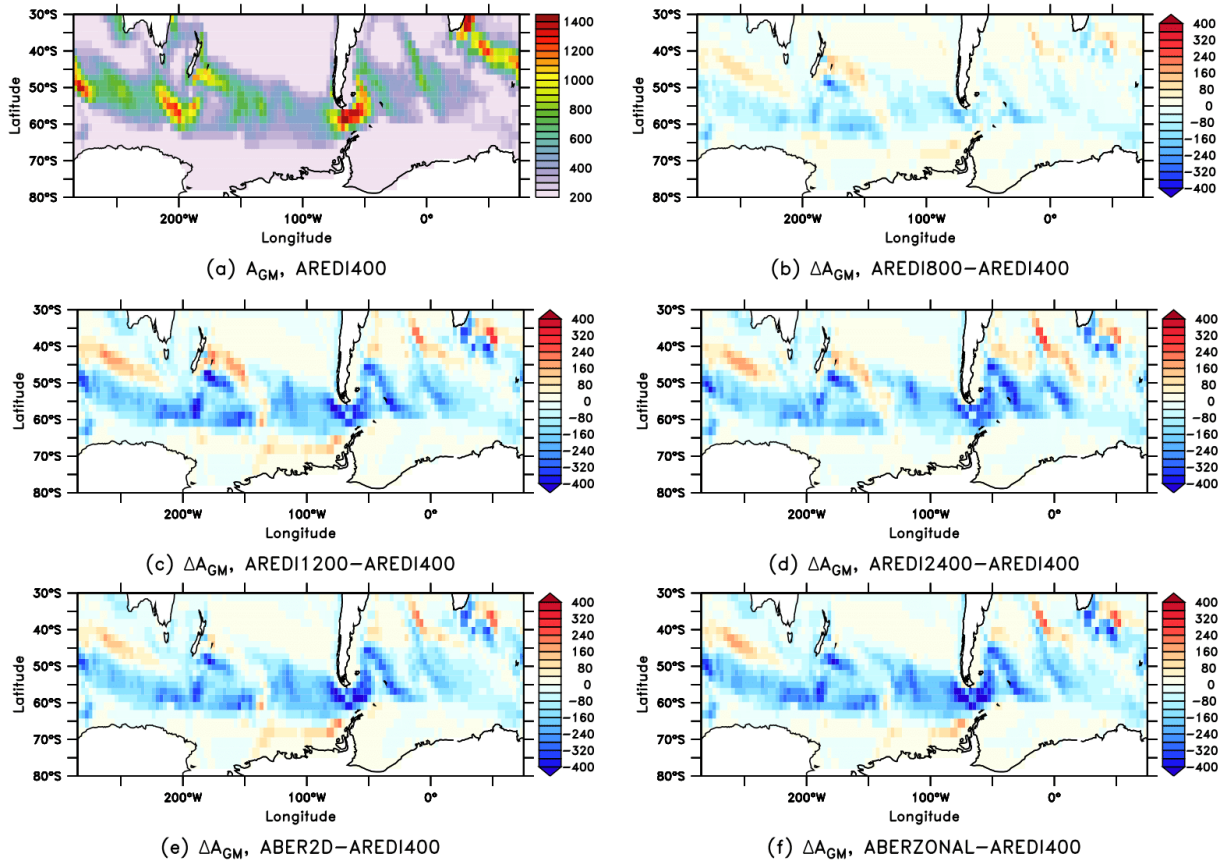
777 FIG. 3. Differences between high mixing (AREDI2400) and low mixing (AREDI400) cases. (A) Zonal wind
778 stress at the air-sea interface. (B) sea surface temperature. (C) Sea surface salinity.



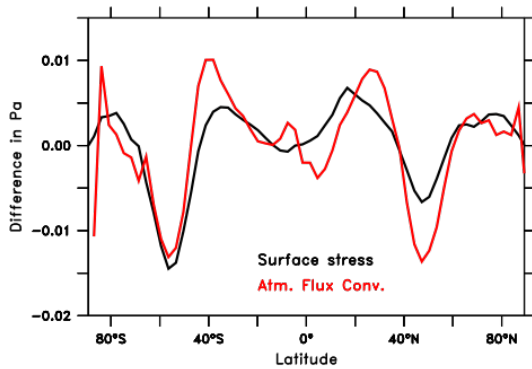
779 FIG. 4. Plots showing zonal (east-west) transport and differences relative to the lowest constant mixing
 780 case anomalies in Sv. (A) AREDI400 transport. (B) transport difference, AREDI800-AREDI400. (C) transport
 781 difference, AREDI1200-AREDI400. (D) transport difference, AREDI2400-AREDI400. (E) transport differ-
 782 ence, ABER2D-AREDI400. (F) transport difference, ABERZONAL-AREDI400.



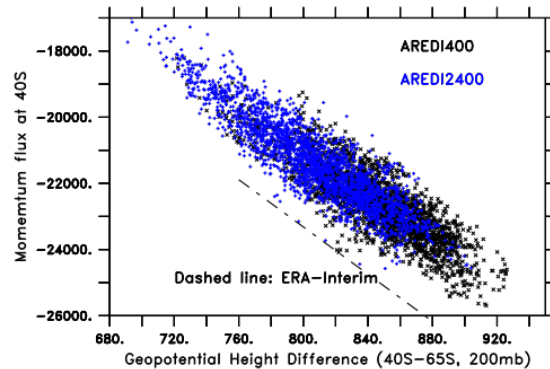
783 FIG. 5. Momentum in the Southern Ocean (A) Zonal mean velocity for all six mixing cases is shown from
 784 80°S to 20°S. (B) Zonal mean velocity difference relative to AREDI400 for the other 5 cases. (C) Zonal mean
 785 wind stress in Pa, NCEP observations shown by the thick black line with symbols. (D) Zonal mean zonal wind
 786 stress difference relative to AREDI400 for the other 5 cases.



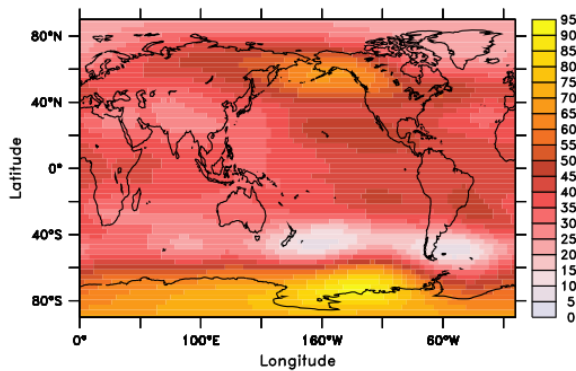
787 FIG. 6. Gent McWilliams coefficients A_{GM} in the Southern Ocean across the model suite. (A) AREDI400
 788 simulation. (B) difference in A_{GM} AREDI800-AREDI400 (C) difference in A_{GM} AREDI1200-AREDI400 (D)
 789 difference in A_{GM} AREDI2400-AREDI400 (E) difference in A_{GM} AREDI800-ABER2D (F) difference in A_{GM}
 790 AREDI800-ABERZONAL.



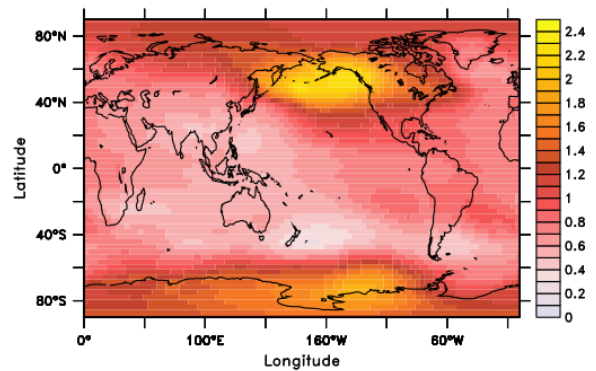
(A) Δ Momentum flux, AREDI2400–AREDI400



(B) Momentum flux vs. $\Delta\Phi_{200}$

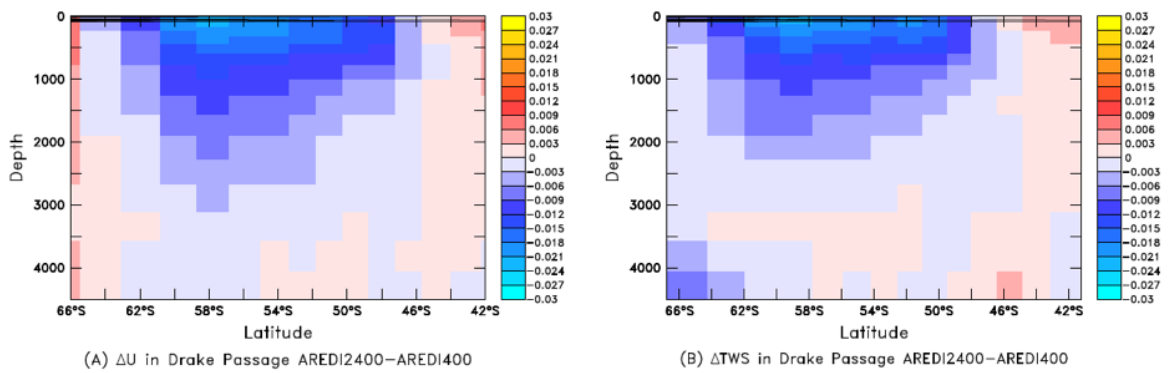


(C) Δ 200mb Geopotential Height

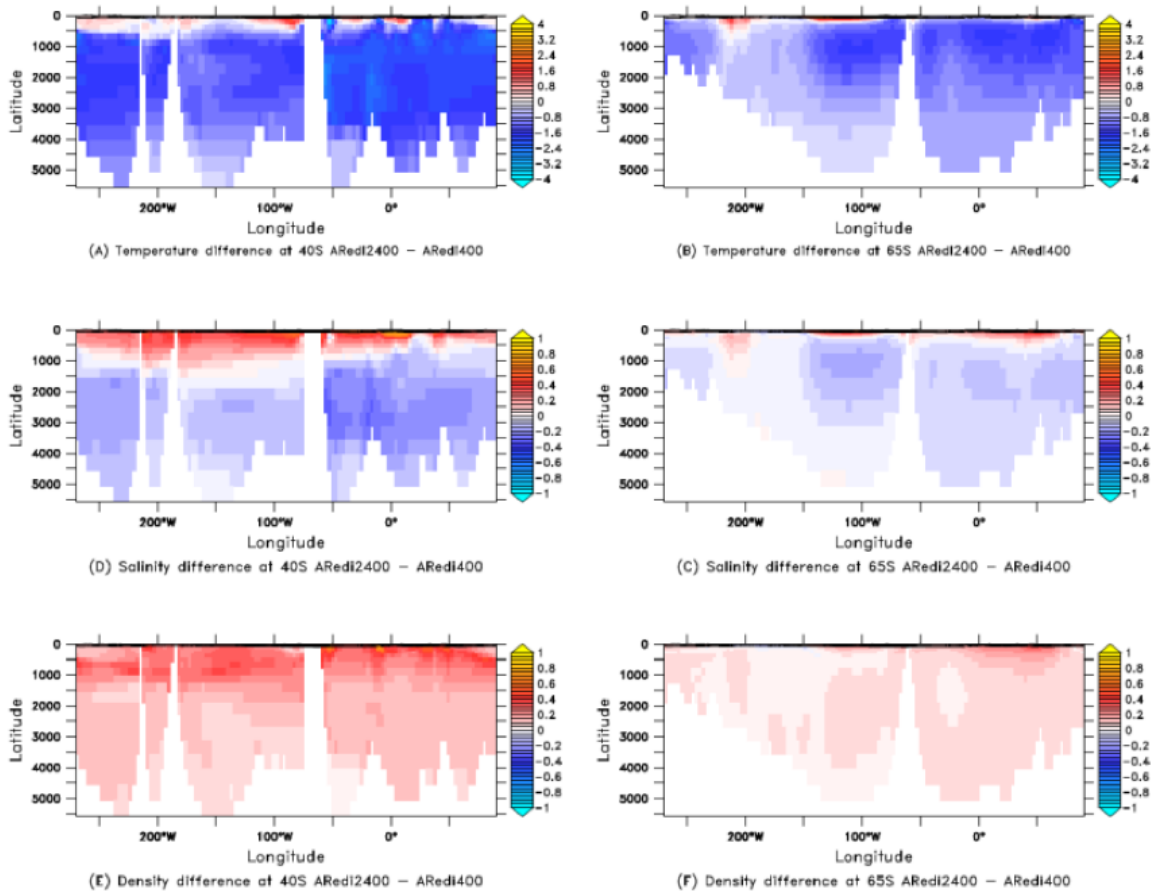


(D) Δ Temp below 200mb

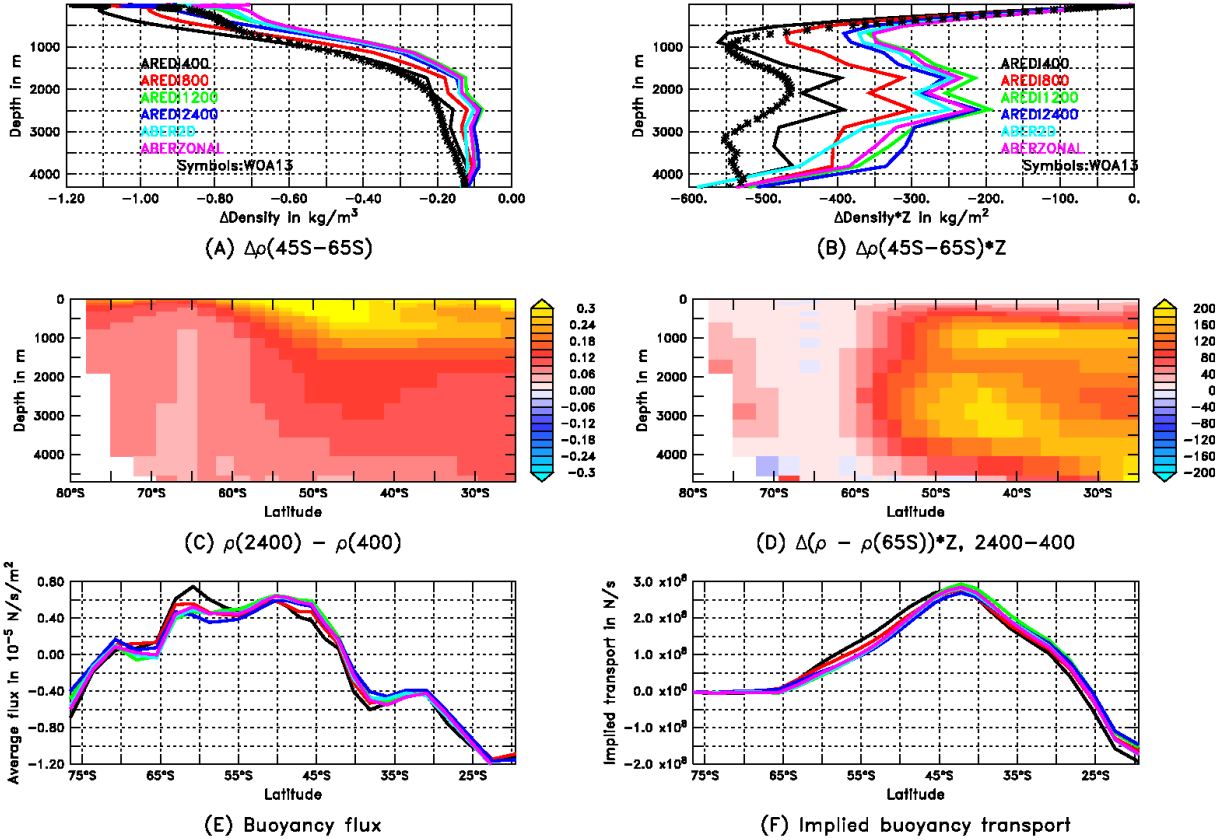
791 FIG. 7. Dynamically relevant changes in the atmosphere between AREDI2400 and AREDI400. (A) Changes
 792 in momentum transport. Black line shows change in surface wind stress. Red line shows change in momentum
 793 flux convergence. (B) Relationship between momentum flux at 40S and geopotential height difference between
 794 40°S and 65°S. Symbols show AREDI400 (black) and AREDI2400 (blue). Dashed line shows equivalent range
 795 and slope of relationship in ERA-Interim reanalysis. (C) Change in 200 mb geopotential height, illustrating
 796 increase over Antarctica. (D) Change in temperature at heights below (pressures above) 200 mb illustrating
 797 connection between increase in geopotential height and surface warming.



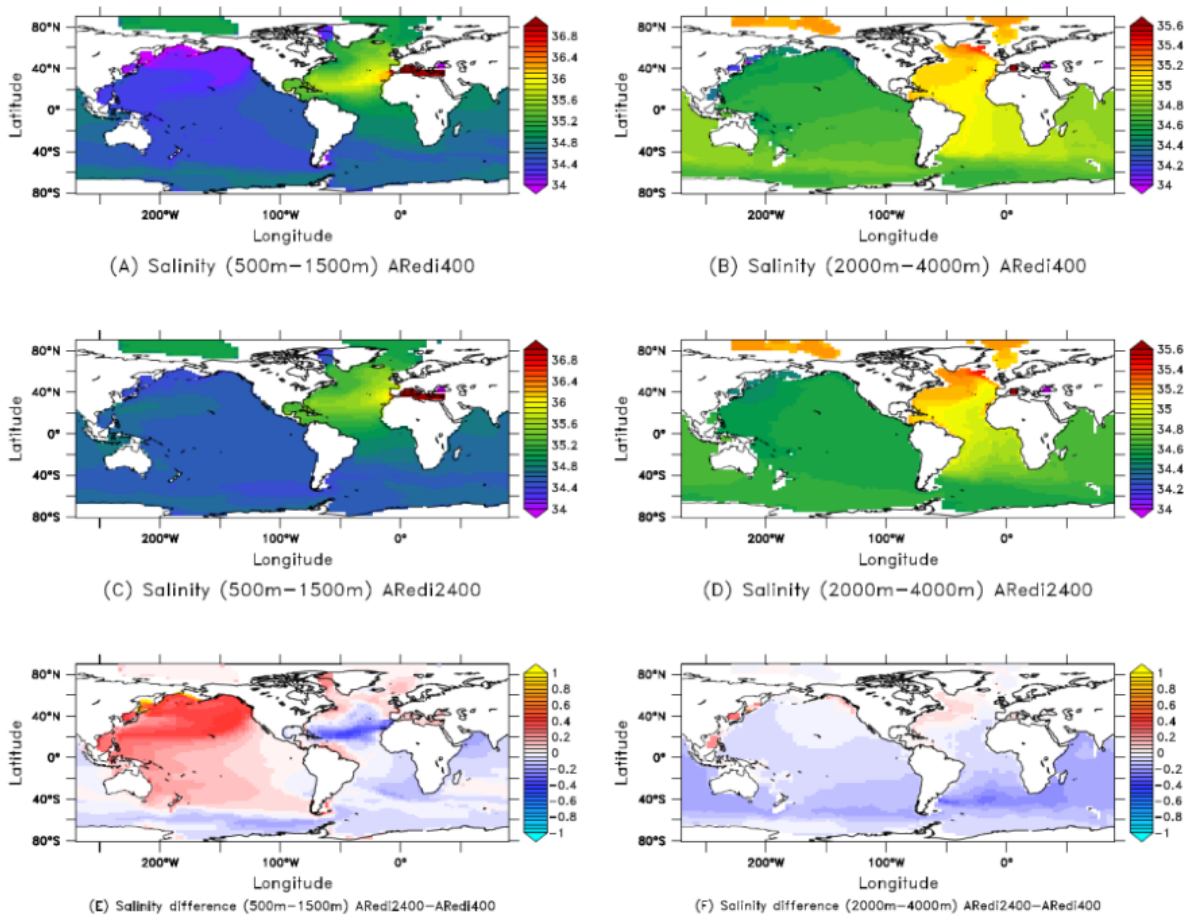
798 FIG. 8. Comparison of changes between AREDI2400 and AREDI400 case. (A) Zonal mean velocity. (B)
 799 Velocity change relative to 4500 *m* computed from thermal wind shear.



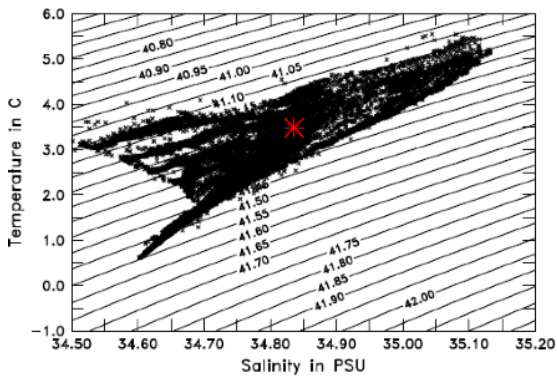
800 FIG. 9. Circumpolar cross sections of changes between AREDI2400 and AREDI400 in potential temperature
 801 (top row), salinity (middle row) and in-situ density (bottom row). The left-hand column shows changes at 40°S
 802 while the right-hand column shows changes at 65°S.



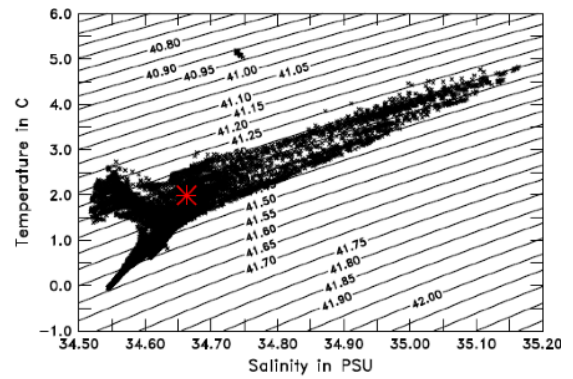
803 FIG. 10. (A) Profiles of zonally averaged difference in density between 45°S and 65°S for each simulation and
 804 observations. (B) Profiles of zonally averaged difference in density between 45°S and 65°S multiplied by depth,
 805 highlighting locations most important for changing the baroclinic transport. (C) Zonally averaged change in
 806 density relative to 65°S between AREDI2400 and AREDI400. (D) Zonally averaged change in density relative
 807 to 65°S multiplied by depth (E) Zonally averaged surface buoyancy flux. (F) Cumulatively integrated buoyancy
 808 flux, indicating transport that would be required to balance the fluxes in (E).



809 FIG. 11. Salinity fields at 500 – 1500 *m* (left column) and 2000 – 4000 *m* (right column). Top row shows
 810 values for AREDI400, middle AREDI2400 and bottom the difference between the two. Note that the increase
 811 in Pacific sector salinity within the Southern ocean shallower depths can be tracked back to the North Pacific,
 812 while the differences at greater depth are largest within the Southern Ocean.

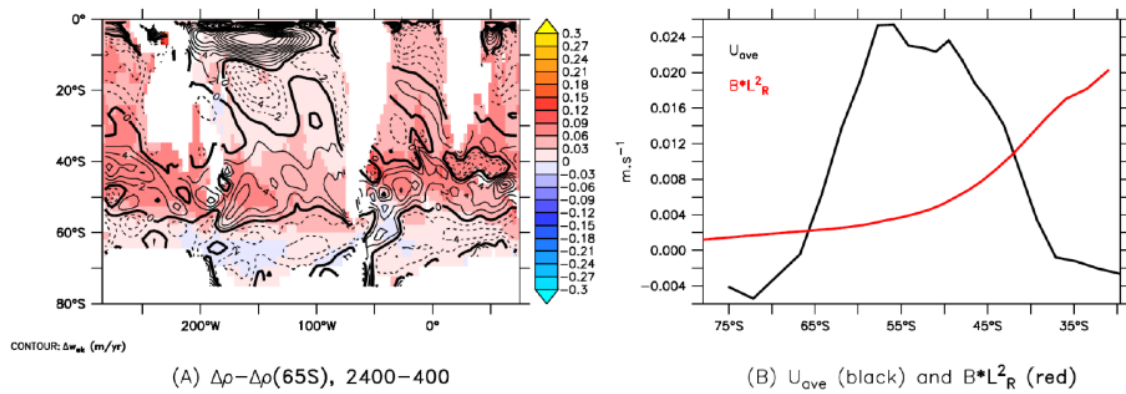


(A) T-S Plot 60S-0, AREDI400



(B) T-S Plot 60S-0, AREDI2400

813 FIG. 12. T-S plots for the Southern Hemisphere from 60°S to the equator in the AREDI400 model (A) and
 814 AREDI2400 model (B). Contours show potential density referenced to 3000 m. Red star shows average value at
 815 40°S.



816 FIG. 13. Explaining deep density changes. (A) Southern hemisphere changes in density at 400 *m* (colors)
 817 overlaid with contours of wind stress curl showing that the most intense changes are found in latitudes with
 818 positive anomalous wind stress curl. (B) Comparison of zonally and depth-averaged velocities (black line) and
 819 zonally averaged Rossby wave speed (red line), showing that between about 65°S and 40°S the mean veloci-
 820 ties exceed the 1st baroclinic Rossby wave speed and so changes in wind stress curl would be expected to be
 821 communicated to the bottom.